*J. Fluid Mech.* (1991), *vol.* 231, *pp.* 361–394
*Printed in Great Britain*



# Linear-eddy modelling of turbulent transport. Part 6. Microstructure of diffusive scalar mixing fields

By ALAN R. KERSTEIN
Combustion Research Facility, Sandia National Laboratories, Livermore, CA 94551-0969, USA

(Received 28 December 1990)

The linear-eddy approach for modelling molecular mixing in turbulent flow involves stochastic simulation on a one-dimensional domain with sufficient resolution to include all physically relevant lengthscales. In each realization, molecular diffusion is implemented deterministically, punctuated by a sequence of instantaneous, statistically independent 'rearrangement events' (measure-preserving maps) representing turbulent stirring. These events emulate the effect of compressive strain on the scalar field. An inertial-range similarity law is incorporated.

The model reproduces key features of scalar power spectra, including dependences of spectral amplitudes and transition wavenumbers on Reynolds and Schmidt numbers. Computed scaling exponents governing scalar power spectra, higher-order fluctuation statistics such as structure functions, and the spatial distribution of scalar level crossings are close to measured exponents. It is inferred that the characterization of stirring as a sequence of independent events (the model analogue of eddies) leads to a useful representation of mixing-field microstructure.

## 1. Introduction

Characterization of the fluctuating concentration field of a diffusive species in turbulent flow is a problem distinct from, though related to, the problem of characterizing turbulent transport. The former problem is more challenging in some respects, since molecular mixing in turbulence is sensitive to fine-scale as well as large-scale motions, while turbulent transport depends mainly on large-scale motions. Molecular mixing measurements can therefore provide stringent tests of turbulence models (Dimotakis 1989*a*).

The problem of molecular mixing in turbulence can be analysed from several viewpoints. At present the only fully systematic approach is direct numerical simulation, in which the Navier–Stokes and molecular-transport equations are solved with sufficient resolution to approximate the exact evolution (Eswaran & Pope 1988; McMurtry & Givi 1989; Kerr 1990). Other approaches, involving modelling assumptions that are *ad hoc* to some extent, can be grouped into two categories: computational models intended to be flexible tools, and conceptual models addressing specific issues.

The first category includes the coalescence–dispersion (Curl 1963), two-particle-dispersion (Durbin 1980) and stirred-reactor (Baldyga & Bourne 1984*a*, *b*) approaches. These approaches have been implemented as stand-alone models exemplified, respectively, by the work of Pratt (1976), Thomson (1990) and Baldyga &

Bourne (1984*c*). Curl's model has also been implemented as a subgrid-scale model coupled to a statistical model representing large-scale processes (Pope 1985).

The second category includes the lognormal (Gurvich & Yaglom 1967; Van Atta 1971), beta (Frisch, Sulem & Nelkin 1978; Antonia *et al.* 1984) and gamma (Andrews & Shivamoggi 1990) models, which focus on intermittency statistics and related aspects of the concentration field. This category also includes models that do not address microstructural aspects but focus on the dependence of overall mixing rates on Reynolds number (*Re*) and Schmidt number (*Sc*) in free shear flows (Broadwell & Breidenthal 1982; Broadwell & Mungal 1988; Dimotakis 1989*b*).

Spanning these categories are the closure models. One-point closures (Shih, Lumley & Chen 1990) are applicable to various flows of interest but address a limited number of measurable quantities, while two-point closures (Lesieur 1987) address a variety of phenomena but are tractable only for the simplest flow configurations.

This partial catalogue indicates the variety of approaches that have proved useful in addressing various aspects of molecular mixing in turbulent flow. The modelling approach adopted here is motivated by the desirability of preserving the mechanistic distinction between the two processes, fluid motion and molecular diffusion, that jointly govern turbulent mixing (Leslie 1973). Namely, fluid motion rearranges the spatial locations of fluid elements without changing species concentrations within those elements, while molecular diffusion causes the exchange of species between neighbouring fluid elements. This author has introduced the linear-eddy modelling approach (Kerstein 1986, 1988, 1989, 1990, 1991*a*, *b*) as a means of capturing this mechanistic distinction in a formulation that incorporates relevant properties of turbulent transport.

It is instructive to note first how other modelling approaches typically treat molecular mixing. In formulations with explicit spatial structure, fluid elements that are sufficiently close to each other based on a fluid-mechanical criterion are molecularly mixed either instantaneously, or at a rate that may be based on a fluid-mechanical timescale. The appropriate lengthscale for many problems is the Kolmogorov scale $l_K$ marking the transition from the inertia-dominated to the viscous-dominated range of lengthscales. This lengthscale is appropriate because it marks a transition from an algebraic to an exponential rate of lengthscale compression (Batchelor 1959). The accelerated compression below $l_K$ causes molecular mixing to be effectively instantaneous for many purposes. In formulations that cannot resolve $l_K$ affordably, a coarser proximity criterion is adopted and molecular mixing is typically implemented at a finite rate representing the time required to reduce the characteristic lengthscale to $l_K$. Though adequate for many purposes, such an approach omits mixing phenomena that may affect transient evolution, concentration-field microstructure, and the dependence of mixing properties on *Sc*.

A more sophisticated approach, the Lagrangian-history direct-interaction approximation, captures key spectral properties of the scalar mixing field in the principal *Sc* regimes (Kraichnan 1968; Leslie 1973), but the computational cost of this non-Markovian two-point closure limits its applicability. The success of this approach indicates the benefits of characterizing the ensemble of fluid-element time-histories in a manner that preserves the mechanistic distinction between molecular and convective effects. The two-particle-dispersion approach achieves a more economical, Markovian formulation by statistically characterizing the time-histories of the relative motions of fluid elements and of molecules within fluid elements. Though successful in many respects (Sawford & Hunt 1986; Thomson 1990), this

approach does not fully reflect the mechanistic distinction between molecular and convective processes. This limitation impacts the treatment of $Sc$ effects, as discussed elsewhere (Kerstein 1988).

These considerations highlight the modelling challenge, namely to achieve a reduced description of turbulent mixing that is economical (in particular, Markovian) and that involves physically sound representations of molecular diffusion as well as fluid motion. To achieve the latter objective, all relevant lengthscales of the concentration field are resolved in the present formulation, allowing direct implementation of molecular diffusion. Economical implementation is achieved by formulating the model in one spatial dimension. The key to the present approach is the one-dimensional ('linear-eddy') representation of fluid motion that is adopted. This aspect is discussed in detail in §2.

In addition to the aforementioned conceptual advantages of capturing time-history effects, the present approach allows the extraction of a wide variety of mixing-field statistics in a manner analogous to experimental data reduction. Thus, a formulation is obtained that is broader in scope than previous models, addressing mixing-field intermittency and related higher-order effects as well as spectral scalings. Related formulations based on the linear-eddy approach have been generalized to accommodate transient and spatially varying turbulent flow-fields, multiple species, and variable-density reacting flows with finite-rate chemistry (Kerstein 1988, 1989, 1990, 1991*a*).

The present concern is the microstructure of incompressible turbulent mixing fields with passive, diffusive scalar contaminants, as reflected by the probability density function (p.d.f.) and the power spectrum of the scalar and its dissipation rate, by higher-order fluctuation statistics such as structure functions and generalized dimensions, and by the stochastic geometry of scalar interfaces. Scaling properties of these quantities are independent of empirical coefficients relating model parameters to physical quantities, so comparison of computed and measured scaling exponents provides an unambiguous test of the model.

The paper is organized as follows. First, the model formulation is presented and physical implications are discussed. Next, properties of computed p.d.f.s are examined. This is followed by comparisons of computed and measured spectral properties, higher-order statistics, and related quantities. Finally, the conceptual and practical implications of the results are assessed.

## 2. Model formulation

The foregoing considerations motivate the formulation of the model in terms of two concurrent processes representing the respective influences of molecular diffusion and fluid motion. The model is implemented on a one-dimensional spatial domain denoted as the interval $0 \leqslant x \leqslant X$. The concentration field $c(x,t)$ evolves from a specified initial condition $c(x,0)$ according to Fick's law,

$$\frac{\partial c}{\partial t} = D_{\mathrm{M}} \frac{\partial^2 c}{\partial x^2}, \tag{1}$$

where $D_{\mathrm{M}}$ is the molecular diffusivity. This deterministic evolution, representing molecular diffusion, is punctuated by instantaneous 'rearrangement events', which may be viewed as representing the effect of individual eddies on the concentration field. Each event is a measure-preserving map of a spatial segment of the

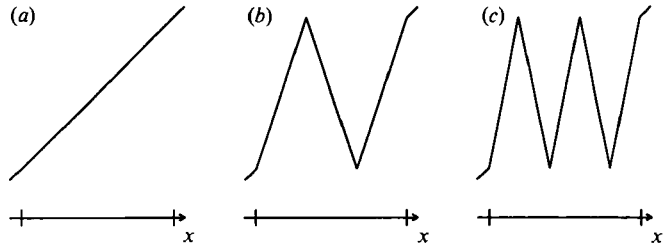


FIGURE 1. Alternative maps representing the effect of an individual eddy. (*a*) Scalar field $c(x,t)$ prior to map. In this example, $c$ is linear in the spatial coordinate $x$. (*b*) Scalar field after applying the triplet map to the segment denoted by ticks. (*c*) Scalar field after applying the quintuplet map to the original scalar field.

concentration field onto itself. The measure-preserving property assures that the species concentration $c$ within any notional 'fluid element' (adopting Lagrangian terminology) is unaffected by the event. Three random variables govern each event: the epoch and location of the event, and the size of the affected segment. The model formulation is completed by specifying the distributions of these random variables, the mapping rule, and the initial and boundary conditions.

Before proceeding, the motivation for representing fluid motion as a sequence of instantaneous events rather than a continuous process is noted. In one dimension, an incompressible fluid can obey the continuity equation only in the trivial case of spatially constant velocity at each instant. (Models that compute the time evolution of ensemble statistics rather than individual realizations can circumvent the issue of continuity within a realization.) To introduce non-trivial fluid motions, spatial non-locality must be allowed. A spatially non-local but temporally continuous process might involve, e.g. a piecewise constant velocity field with non-local fluid displacements from points of negative velocity discontinuity to points of positive discontinuity. Such a process would introduce discontinuities into concentration fields that are continuous initially. This artifact might be acceptable for some purposes (previous linear-eddy formulations were subject to such an artifact), but it can be avoided in the framework of a temporally discontinuous process.

The mapping rule adopted here is the 'triplet map' (Kerstein 1991*a*, *b*), whose effect on the scalar field $c(x) = x$ is illustrated in figure 1. The scalar field within the chosen segment is compressed (as by photographic reduction) by a factor of three, thus tripling the scalar gradient throughout the segment. The original scalar field within the segment is then replaced by three adjacent copies of this compressed field, with the middle copy mirror-inverted. Formally, application of this map to the segment $[x_0, x_0+l]$ at time $t_0$ transforms $c(x,t_0)$ to $\hat{c}(x,t_0)$ according to

$$\hat{c}(x,t_0) = \begin{cases} c(3x-2x_0,t_0) & x_0 \leqslant x \leqslant x_0+\frac{1}{3}l \\ c(-3x+4x_0+2l,t_0) & x_0+\frac{1}{3}l \leqslant x \leqslant x_0+\frac{2}{3}l \\ c(3x-2x_0-2l,t_0) & x_0+\frac{2}{3}l \leqslant x \leqslant x_0+l \\ c(x,t_0) & \text{otherwise.} \end{cases} \tag{2}$$

This map does not cause any spurious discontinuities of $c(x,t)$ (though it does introduce discontinuities of $\partial c/\partial x$, whose impact is considered in §4.1). The map causes a multiplicative increase of the scalar gradient throughout the size-$l$ segment, analogous to the effect of compressive strain in turbulent flow. The multiplicative random process induced by a sequence of such events is the basis of the scaling

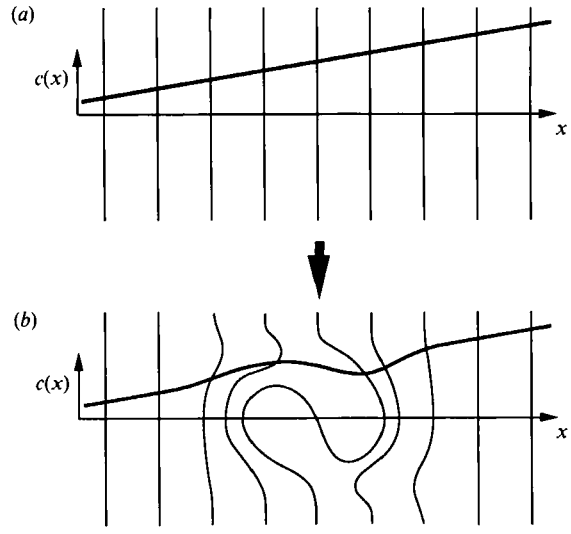


FIGURE 2. Schematic illustration of the effect of a single, clockwise eddy on a two-dimensional scalar field that initially has a uniform concentration gradient. (*a*) Initial concentration isopleths (vertical lines) and concentration profile $c(x)$ (heavy line) parallel to the initial concentration gradient. (*b*) Concentration isopleths and concentration profile at a later time.

properties of the model. In this regard, the model is analogous to a two-dimensional picture of turbulent mixing based on the generalized baker's map (Ott & Antonsen 1989).

Computed results are based on the triplet map except where stated otherwise. An alternative map, the 'quintuplet map' illustrated in figure 1(*c*), is employed in some computations to determine the sensitivity of the results to the choice of map. This map, an obvious extension of the triplet map, is the second in a series of higher '*n*-tuplets' that can be defined.

The intuitive rationale for adopting the triplet map is illustrated in figure 2. Consider the effect of a single, clockwise eddy on a two-dimensional concentration field that initially (figure 2*a*) has a uniform gradient. The eddy distorts the concentration isopleths, which are linear initially, as indicated in figure 2(*b*). Taking the $x$-direction to be parallel to the initial gradient, the linear initial profile evolves to a form qualitatively resembling the profile obtained by applying the triplet map to the linear profile (figure 1*b*).

This comparison motivates the analogy between the triplet map and the action of a single eddy, providing a physical basis for specifying the random processes governing the sequence of rearrangement events. Another analogy, between the transport induced by the rearrangement process and the turbulent diffusivity, is also required. These analogies have two implications with regard to the model. First, a random sequence of rearrangement events induces a random walk of a fluid element, with an associated diffusivity that is interpreted as the turbulent diffusivity $D_T$. This interpretation leads to a relationship between an event-frequency parameter and the physical quantity $D_T$, as demonstrated shortly. Secondly, an aspect of turbulent flow-field microstructure is incorporated into the model by requiring that rearrangement events involving segments of size $l$ or less obey the transport scaling governing eddies in that size range. Namely, the Kolmogorov cascade picture of inertial-range turbulent transport requires that the diffusivity induced by eddies of size $l$ or less be proportional to $l^p$, where $p = \frac{4}{3}$ (Tennekes & Lumley 1972).

Furthermore, the eddy sizes are confined to the range $L_K \leqslant l \leqslant L$, where $L$ and $L_K$ are the model analogues of the integral and Kolmogorov lengthscales of the turbulent flow. These considerations suffice to complete the formulation of the model in terms of the quantities $D_M$, $D_T$, $p$, $L$ and $L_K$. (The symbol $p$ is retained because values other than $\frac{4}{3}$ are considered. Computed results are based on $p = \frac{4}{3}$ unless stated otherwise.)

In the present formulation, rearrangement events are statistically independent. For each event, the parameter $x_0$ in (2) determining the spatial location of the event based on (2) is selected according to the uniform distribution over the spatial domain $[0, X]$. (The map extends beyond $X$ if $x_0 > X - l$. This situation is handled by means of a jump-periodic boundary condition, discussed shortly.) Epochs $t_0$ are governed by a Poisson process with rate $\lambda X$, where the event-frequency parameter $\lambda$ has units (length × time)$^{-1}$. Segment sizes $l$ are selected according to a p.d.f. $f(l)$.

$\lambda$ and $f(l)$ are expressed in terms of the five input quantities as follows. The fluid-element diffusivity, derived in terms of $\lambda$ and $f(l)$ in the Appendix, is set equal to $D_T$, giving

$$D_T = \tfrac{2}{27}\lambda \int_0^\infty l^3 f(l)\, dl. \tag{3}$$

The diffusivity attributable to segments of size $l$ or less is obtained by replacing the upper limit of integration by $l$. In the inertial range $L_K \ll l \ll L$, that diffusivity scales as $l^p$ provided that $f(l)$ scales as $l^{p-4}$. Therefore the segment-size p.d.f. is taken to be

$$f(l) = \frac{3-p}{L[(L/L_K)^{3-p} - 1]} \left(\frac{l}{L}\right)^{p-4}, \tag{4}$$

confined to the range $L_K \leqslant l \leqslant L$, where the prefactor follows from the normalization condition. Substitution of (4) into (3) yields the expression

$$\lambda = \frac{27}{2} \frac{p}{3-p} \frac{D_T}{L^3} \frac{(L/L_K)^{3-p} - 1}{1 - (L_K/L)^p}. \tag{5}$$

It is convenient to scale length and time with respect to $L$ and the 'large-eddy turnover time' $T_L = L^2/D_T$. It is evident from (1), (4) and (5) that scaled quantities depend only on $p$, $L/L_K$ and $D_T/D_M$. In comparisons to measurements, $p$ is fixed at $\frac{4}{3}$, although other values are considered for the purpose of sensitivity analysis. Dependences on the other two quantities are parameterized by $Re_S \equiv (L/L_K)^{\frac{4}{3}}$ and $Sc_S \equiv (D_T/D_M)/Re_S$, the nominal Reynolds and Schmidt numbers of the simulation. The former definition reflects the functional dependence of the Reynolds number on $L/L_K$ that is prescribed by the Kolmogorov inertial-range cascade (Tennekes & Lumley 1972). The latter definition reflects the identification of the ratio $D_T/D_M$ with the physical quantity $ReSc/Pr_T$, where the Reynolds number $Re$ is the ratio $\nu_T/\nu$ of turbulent to molecular viscosity, $\nu/D_M$ is the Schmidt number $Sc$ (or the Prandtl number $Pr$ when referring specifically to the temperature field), and the turbulent Prandtl number $Pr_T = \nu_T/D_T$ is an empirical quantity (Hinze 1975).

The definitions of $Re_S$ and $Sc_S$ are motivated by a kinematical analogy between the model and turbulent mixing. The model involves neither a flow field nor viscosity *per se* and yet it reproduces many of the effects usually associated with those dynamical aspects.

In §4.2, $Re_S$ and $Sc_S$ are expressed in terms of the physical quantities $Re$ and $Sc$ based on empirical coefficients of proportionality. Many properties considered here are not sensitive to $Re$ or $Sc$ (provided that an appropriate asymptotic limit with

respect to these parameters is approached) and therefore do not depend on the empirical inputs determining the coefficients of proportionality.

With the model thus specified (apart from initial and boundary conditions, discussed shortly), the analogy between rearrangement events and eddies can be developed in more detail. Inertial-range transport properties are 'built into' the model through (4) and (5). Key mixing properties follow from those equations and from the definition of the triplet map.

The main features of the triplet map are the tripling of the scalar gradient within each fluid element of the chosen segment, and the mapping of each compressed element onto three daughter images. A stationary random sequence of such events induces two effects analogous to the key properties of turbulent mixing. First, scalar gradients increase exponentially with an $e$-folding time of order $(\lambda L_{\mathrm{K}})^{-1}$. For $Re_{\mathrm{S}} \gg 1$, this is of the order of the model Kolmogorov time $T_{\mathrm{K}} = Re_{\mathrm{S}}^{-\frac{1}{2}} T_{\mathrm{L}}$ according to (5) and the definitions of $Re_{\mathrm{S}}$ and $T_{\mathrm{L}}$. Secondly, each map triples the number of crossings of a given concentration level within a segment. These crossings correspond to intersections of a concentration isopleth by the segment, and each tripling represents a tripling of the isopleth surface associated with the segment. Thus, the rearrangement process induces exponential growth of isopleth area, again with an $e$-folding time of order $T_{\mathrm{K}}$. These two interrelated properties are in accordance with classical theory (Batchelor 1952, 1959). The manifestation of these properties along the computational line is evident in figure 2, which illustrates the compressive action of the stirring motion, accompanied by isopleth extension and distortion, and the consequent modification of $c(x)$.

Based on these observations, it is evident that the rearrangement process, in conjunction with molecular diffusion implemented according to (1), has the potential to reproduce the structural properties of turbulent mixing fields. The objective of the present study is to determine the extent to which this potential is realized. To this end, a simple initial-boundary-value problem is formulated whose scalar fluctuation statistics relax to a homogeneous, statistically steady state, thereby avoiding complications such as transient evolution of the system.

Statistically steady scalar fluctuations cannot be maintained in a closed finite domain because molecular diffusion dissipates scalar fluctuations and the system eventually relaxes to constant $c$. Therefore an infinite domain is considered. The concentration field $c(x,t)$ evolves in time from the initial condition $c(x,0) = Gx$ for $-\infty < x < \infty$, where $G$ is an imposed scalar gradient. By symmetry, the ensemble average $\langle c(x,t)\rangle$ neither increases nor decreases from its initial value, so $\langle c(x,t)\rangle = Gx$ for all $t$. Since the mean scalar gradient is thus maintained, turbulent stirring provides an ongoing source of scalar fluctuations to counterbalance the dissipative effect of molecular diffusion, and a non-trivial statistically steady state is obtained after a transient period. The concentration field $c(x+a,t)$ is statistically equivalent to the concentration field $c(x,t)+Ga$, so steady-state statistical properties depend on neither $x$ nor $t$. In particular, the mean-subtracted concentration field $c'(x,t) = c(x,t)-Gx$ is spatially homogeneous. With one exception discussed in §6, statistics are computed with respect to $c'(x,t)$.

This configuration cannot be realized literally in a laboratory experiment, but it is emulated in laboratory or geophysical flows in which a uniform transverse gradient of mean temperature (or other diffusive contaminant) is established over a distance much larger than the turbulence integral scale. Between the scalar relaxation time (of the order of the large-eddy turnover time) and the time for turbulent transport of fluid across the constant-gradient zone, the scalar fluctuation field in such a flow

is spatially homogeneous and statistically steady to a good approximation, provided that the turbulent stirring field is spatially homogeneous and statistically steady. The latter proviso is difficult to satisfy in practice. Nevertheless, many scaling predictions based on homogeneous, statistically steady turbulence are confirmed experimentally over a wide range of flow conditions.

Numerical simulations, like laboratory experiments, are limited to finite domains. However, simulations can be implemented on a bounded domain, here chosen to be $0 \leqslant x \leqslant X$, in a manner that is equivalent to the unbounded formulation with constant mean scalar gradient $G$ by employing a jump-periodic boundary condition. Namely, the scalar value $c(x,t)$ at given $x$ in the range $[0,X]$ determines the scalar value at $x+kX$ according to $c(x+kX,t) = c(x,t)+kXG$, where $k$ is any integer (positive or negative).

Though the present study is limited to this simple configuration, the modelling approach allows the study of more general transient and spatially inhomogeneous configurations as well. More general formulations are obtained by choosing alternative initial and boundary conditions, by allowing $L$ and $Re_S$ to vary with $x$ and $t$, and by supplementing the two processes of molecular diffusion and spatial rearrangement by additional processes, which may be deterministic or stochastic. Examples of such applications appear elsewhere (Kerstein 1989, 1990, 1991*a*, *c*).

Thus far, the model has been formulated with respect to continuous variables $x$ and $t$. On a discretized computational domain, finite-difference numerical solution of (1) is straightforward. The discrete version of the triplet map is defined so as to satisfy species conservation exactly in the discrete implementation. The discrete triplet map is defined for segments whose size is an integer multiple of three computational cells. The discrete map, applied to a segment consisting of $3k$ cells sequentially labelled $1, 2, \ldots, 3k$, yields the sequence $1, 4, 7, \ldots, 3k-8, 3k-5, 3k-2, 3k-1, 3k-4, 3k-7, \ldots, 8, 5, 2, 3, 6, 9, \ldots, 3k-6, 3k-3, 3k$. For example, a segment consisting of six cells sequentially labelled 1, 2, 3, 4, 5, 6 is rearranged to obtain 1, 4, 5, 2, 3, 6.

Quantitative predictions are obtained from the model by exact analysis, by scaling arguments, and by numerical implementation as a Monte Carlo simulation. The results presented here are based primarily on numerical simulation, supplemented by exact analysis or scaling arguments where possible.

Computed results may differ from exact properties of the model due to finite-sample effects (i.e. statistical precision), numerical roundoff error, and spatial and temporal discretization. In §5, the impact of these errors on the higher-order statistics most sensitive to such errors is assessed.

Each computed realization evolves from the initial condition $c(x,0) = x/L$ on the finite domain $[0,L]$, with the jump-periodic boundary condition applied. (Scaled quantities are not affected by the assignment $G = 1/L$. The size of the computational domain is chosen to allow investigation of microstructure at lengthscales below the integral scale $L$. In studies addressing large-scale entrainment phenomena, domains larger than $L$ are employed.) Each realization relaxes to a statistically steady state after a transient period whose duration typically ranges from $2T_L$ to $5T_L$. (Recall that $T_L = L^2/D_T$.) Subsequently, simulation statistics are gathered over a typical time interval $10T_L$, adjusted upward or downward depending on the precision desired in individual cases. Only one realization is computed per case (defined as the complete set of inputs, including cell size and timestep, needed to specify a computation), except for one random-number-seed sensitivity test. One realization suffices because time averages correspond to ensemble averages in the steady state. (In studies of

transient, spatially inhomogeneous configurations, multiple realizations are generally needed in order to obtain temporally and spatially resolved statistical properties.) For all cases reported here, the spatial domain was discretized into 8192 cells.

Values of $Re_S$ for the computations were chosen to be as high as possible consistent with spatial and temporal resolution requirements and computational affordability. (The typical run time for a computed realization was one hour on a Cray XMP-24. Computations were run-time-limited rather than memory-limited.) The large-$Re_S$ limit is the regime of greatest interest with respect to fundamental scaling properties as well as practical applications. Three values of $Sc_S$ were considered, namely 0.7 (corresponding to $Sc$ for ambient air), 600 (corresponding to $Sc$ for water) and 0.018 (corresponding to $Pr$ for mercury). These values are related to the corresponding $Sc$ or $Pr$ values by a non-unity coefficient of proportionality, which is determined *a posteriori* by comparing computed results to measurements (see §4.2). These values were chosen because they roughly correspond to cases of physical interest, and because they encompass the principal spectral regimes of molecular mixing in turbulence, discussed in §4.1.

Although the model ostensibly simulates mixing-field evolution along a straight line, it is more accurate for some purposes to regard the computational domain as a time-varying space curve locally aligned with the concentration gradient. This interpretation reflects the fact that all rearrangement events involve compression, and that concentration gradients in turbulent flows tend to align locally with the most compressive strain direction (Ashurst *et al.* 1987).

One consequence is that the $x$-derivative of the simulated concentration field should be interpreted as the local concentration gradient rather than its projection onto a fixed laboratory coordinate. Thus, the model analogue of the scalar dissipation rate $2D_M(\nabla c')^2$ is $2D_M(\partial c'/\partial x)^2$. Another consequence is that the power spectrum of the simulated concentration field is the model analogue of the three-dimensional rather than the one-dimensional scalar spectrum. Simulated spectra are therefore compared to measured one-dimensional spectra that have been transformed into three-dimensional spectra using a relation based on local isotropy (Hinze 1975). (The mathematical basis of these assertions concerning the scalar dissipation rate and the power spectrum is presented in the Appendix.)

Many properties of interest depend primarily on the statistical weight and spatial distribution of regions of high scalar gradient. These properties tend to be insensitive to the distinction between averaging over the aforementioned space curves and averaging over a fixed coordinate. However, properties that depend on the statistics of low-gradient regions are sensitive to this distinction for the following reason. On a space curve locally aligned with the concentration gradient, every point of zero concentration derivative along the arc is a zero-gradient point of the concentration field. In contrast, a fixed line has zero probability of intersecting a zero-gradient point of the concentration field (Gibson 1968*a*). Averages over the space curves are, in effect, conditional samples that give disproportionate weight to low-gradient regions. This bias is reflected in model results for the p.d.f. of scalar dissipation (§3) and for certain intermittency statistics (§5).

## 3. Distribution of the scalar and the scalar dissipation rate

Typical computed p.d.f.s of the mean-subtracted concentration $c'$ and of quantities that depend on $Q \equiv L^2(\partial c'/\partial x)^2$ are plotted in figure 3. ($Q$ is a non-dimensional form of the scalar dissipation rate.) Centred differencing is used to compute $x$-derivatives;

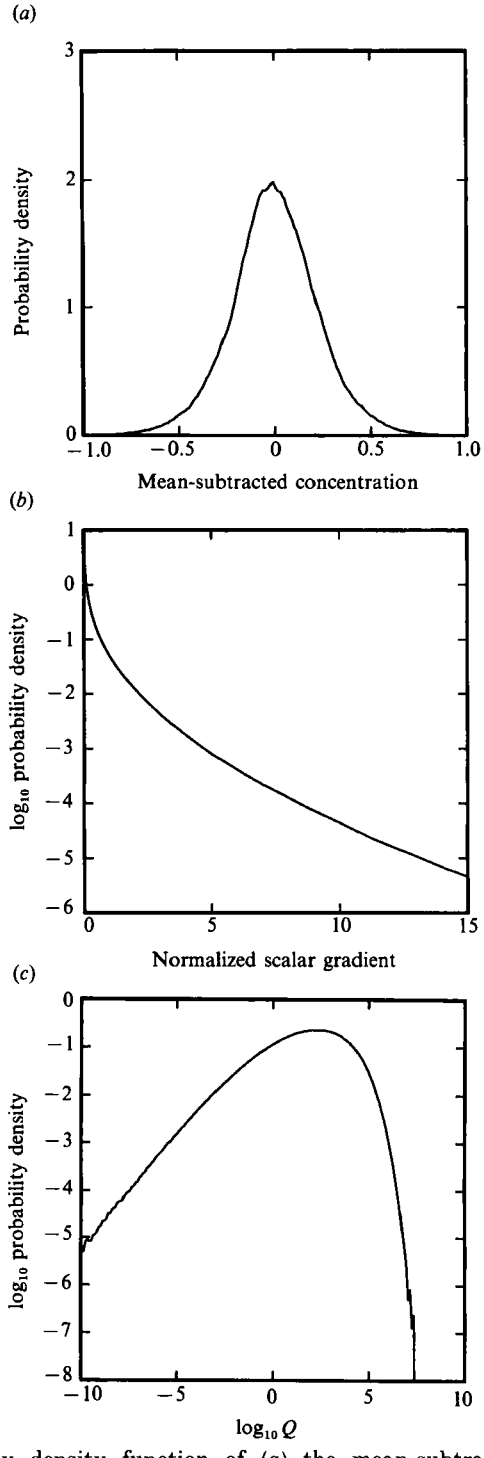


FIGURE 3. Probability density function of (*a*) the mean-subtracted concentration $c'(x,t) = c(x,t) - (x/L)$, (*b*) the normalized scalar gradient $g/\langle g^2\rangle^{\frac{1}{2}}$, where $g \equiv Q^{\frac{1}{2}} \equiv L|\partial c'/\partial x|$, and (*c*) $\log_{10} Q$, computed for $Re_S = 10^4$ and $Sc_S = 0.7$.

first differencing is found to give indistinguishable results for this and all other statistics of the dissipation field.

Computed concentration p.d.f.s are symmetric about $c' = 0$, with flatness factors about 20% above the Gaussian value for all cases considered. The tails of the p.d.f.s are found to be Gaussian. The latter result is an artifact of the configuration simulated here, in which a jump-periodic boundary condition is imposed on a domain of size $L$. Computations have also been performed on domains much larger than $L$. These computations, performed for $Re_S$ of order unity, yield p.d.f.s with exponential tails. This result is consistent with a recent (Pumir, Shraiman & Siggia 1991) theoretical analysis that predicts exponential tails for the p.d.f. of a stirred, diffusive scalar subject to a constant mean gradient, irrespective of the Reynolds number of the stirring process.

P.d.f.s of quantities that depend on $Q$ are plotted in figure 3(*b*, *c*). The formats of the plots facilitate interpretation of the large-$Q$ and small-$Q$ behaviours, respectively. The format of figure 3(*b*) is often used to examine the extreme behaviour of spatial differences or derivatives of fluctuating quantities in turbulence (Antonia *et al.* 1984; Kraichnan 1990). That figure is a semilog plot of the p.d.f. of $g = Q^{\frac{1}{2}}$, the scaled derivative of $c'$, for a case in which $Sc_S = 0.7$.

Some features of the computed p.d.f. can be interpreted by analysing the case $Sc_S = \infty$. In this case a steady state is never reached owing to the unabated increase of scalar gradients. Nevertheless, analysis is greatly simplified by the fact that the scalar gradient $g(t)$ in a given fluid element at time $t$ is $3^j g(0)$, where $j$ is the number of rearrangement events that compress the fluid element during $[0, t]$.

Since events are statistically independent, $j$ is governed by the Poisson probability function (Wilks 1962) $\text{Prob}[j = J] = m^J \mathrm{e}^{-m}/J!$, where $m$ is the mean value of $j$ and can be expressed in terms of model parameters as $m = Rt$, where the mean rate of events affecting a given fluid element is $R = \lambda \int lf(l)\,\mathrm{d}l$. The leading-order $g$ dependence at large $g$ is governed by the factorial term in the probability function, which does not depend on $m$. Applying Stirling's approximation and transforming to obtain the p.d.f. of $g(t)$, the large-$g$ tail is found to fall off as $[g/g(0)]^{-\ln\ln[g/g(0)]/\ln 3}$, i.e., faster than any power of $g$ but slower than exponentially.

There is no assurance that this result for the case $Sc_S = \infty$ is applicable to the steady-state regime obtained for finite $Sc_S$. A quantitative test of this subtle functional dependence on $g$ is not computationally affordable, but the inferred slower-than-exponential fall-off can be tested. Finite-$Sc_S$ computations confirm this feature, as illustrated by the p.d.f. plotted in figure 3(*b*). The shape of the p.d.f. roughly corresponds to the shape obtained by Antonia *et al.* (1984) from measurements of a related quantity, the difference between temperature values measured at two neighbouring points in a turbulent gas jet.

Slow fall-off is a general property of p.d.f.s of velocity derivatives as well as scalar derivatives in turbulence (Kraichnan 1990). In this regard, the present analysis highlights the causative role of compressive strain, effectively acting as a multiplicative random process operating on spatial derivatives. This aspect has been recognized in previous work (Gurvich & Yaglom 1967). The precise functional form of the tails of measured p.d.f.s is sensitive to mechanistic details that are not fully understood (Monin & Yaglom 1975; Andrews *et al.* 1989).

In figure 3(*c*), the same p.d.f. is plotted in the format used by Dowling (1991) to highlight the behaviour at low values of the scalar derivative. For derivatives along a fixed line, Dowling notes that the principal contribution to the p.d.f. in this range is from the neighbourhoods of turning points of the scalar. Geometrical considerations

yield a $Q^{-\frac{1}{2}}$ divergence of the p.d.f. of $Q$ in the limit $Q \to 0$. In the format of figure 3(*c*), this behaviour manifests itself as convergence to slope $\frac{1}{2}$ for small $Q$.

This behaviour is an artifact of the model property that zero-gradient points occur in the computations, but do not occur along a fixed line in a three-dimensional scalar field. Therefore the model p.d.f. for small $Q$ is akin to measured p.d.f.s of the squared scalar derivative in a fixed direction. This interpretation does not apply for all $Q$; a more precise interpretation of model statistics as averages over a time-varying space curve is presented at the end of §2. Therefore the p.d.f. transformation (Dimotakis, Broadwell & Zukoski 1990) that relates directional derivatives along a fixed line to gradients of isotropic scalar fields is not applicable here.

## 4. Scalar power spectra

### 4.1. *Spectral ranges and scalings*

As discussed in §2, simulated scalar power spectra are analogous to three-dimensional spectra obtained by transforming measured one-dimensional spectra. The experimental results considered here were reported as three-dimensional spectra and therefore can be compared directly to simulated spectra.

Scalar spectral ranges are classified according to the fluid-mechanical regime (inertial above $l_K$, viscous below $l_K$, where $l_K$ is the Kolmogorov scale) and the presence or absence of molecular influences (Lesieur 1987). Molecular diffusion is effective in counteracting strain-induced growth of scalar gradients at lengthscales $l$ below the Batchelor scale $l_B = Sc^{-\frac{1}{2}} l_K$ for $Sc \geqslant 1$, and below the Obukhov–Corrsin scale $l_C = Sc^{-\frac{3}{4}} l_K$ for $Sc \leqslant 1$. (The qualitative differences between mixing mechanisms above and below $Sc = 1$ are elaborated shortly.)

The scales $l_K$, $l_B$ and $l_C$ demarcate the scalar spectral ranges for various $Sc$. The model analogues $L_B$ and $L_C$ of $l_B$ and $l_C$ are obtained by substituting $Sc_S$ for $Sc$ and $L_K$ for $l_K$, where $L_K$ was defined in §2. The model analogues of the scalar spectral ranges are investigated by scaling analysis and by examination of spectra computed from simulated realizations.

Estimates of spectral and other scaling exponents are obtained from dimensional considerations like those typically applied to molecular mixing in turbulence (Tennekes & Lumley 1972; Lesieur 1987). The estimates are subject to the usual caveat that they omit any intermittency corrections reflecting the fluctuating nature of the concentration field. Intermittency effects are identified by comparing the estimates to exponents obtained from simulated realizations, and by examining other quantities that characterize the intermittency (see §5).

Power spectra $E(k)$ of simulated realizations are computed according to

$$E(k) = \pi^{-1} \int_{-\infty}^{\infty} \langle c'(0)\, c'(x) \rangle \exp(-ikx)\, \mathrm{d}x. \tag{6}$$

It is shown in the Appendix that this definition is the model analogue of the usual definition of the three-dimensional power spectrum (Hinze 1975). The wavelength $l$ associated with the wavenumber $k$ is given by $k = 2\pi/l$. It is convenient to perform the scaling analyses in terms of $l$ and re-express the final results in terms of $k$. According to (6), $E$ scales as $l\delta_l^2$, where $\delta_l$ is the characteristic scalar fluctuation amplitude for wavelengths of order $l$. (For the purpose of scaling analysis, $\delta_l$ is treated as a dimensional quantity although $c'$ is often taken to be a normalized quantity in practice.) Spectral scalings are obtained by estimating the $l$ dependence of $\delta_l$ in the various regimes.

First, it is shown that the model parameters $L_K$, $L_B$ and $L_C$ have meaning analogous to their physical counterparts. $l_K$ is the lengthscale below which molecular viscosity damps inertial energy transfer to smaller scales. The kinematical consequence of this cutoff has been incorporated into the model by adopting a lower cutoff $L_K$ on the range of segment sizes. In §2, this cutoff was parameterized in terms of $Re_S = (L/L_K)^{\frac{4}{3}}$, motivated by the analogous relation between the physical quantities $Re$ and $L/l_K$. The validity of this analogy will be demonstrated by showing that the $Re_S$ scalings of the model are consistent with the $Re$ scalings governing turbulent mixing.

The lengthscale at which molecular-diffusive smoothing of the scalar field counteracts strain-induced wrinkling is estimated by equating the characteristic timescales of the respective processes (Batchelor 1959). The characteristic molecular-diffusion timescale corresponding to lengthscale $l$ is $l^2/D_M$. The usual estimate for the characteristic fluid-mechanical timescale $t_l$ in this context is $l/v_l$, where $v_l$ is a typical velocity fluctuation over a distance $l$. ($t_l$ is the 'turnover time' of a size-$l$ eddy.) The present formulation does not involve a velocity field *per se*. The model analogue of $t_l$ is the time

$$\tau_l \sim \left[\lambda \int_l^L l' f(l')\, \mathrm{d}l'\right]^{-1} \tag{7}$$

between successive rearrangement events of size $l$ or larger that include a given point. (The term in square brackets is a weighted sum over the characteristic rate for size-$l'$ events. Note that the dominant contribution to the rate is from $l'$ in the vicinity of $l$, so $\tau_l$ is an appropriate characteristic time for size-$l$ eddies.) Based on (4) and (5), this gives

$$\tau_l \sim (l/L)^{2-p} T_L \tag{8}$$

for $L_K < l \ll L$. For $l < L_K$, (7) gives $\tau_l \sim (L_K/L)^{2-p} T_L$, independent of $l$.

For $Sc_S > 1$, the balance condition $\tau_l = l^2/D_M$ is satisfied at a lengthscale below $L_K$. Specializing to $p = \frac{4}{3}$, the foregoing results and the definitions of $T_L$, $Re_S$ and $Sc_S$ yield a balance lengthscale of order $L_B = Sc_S^{-\frac{1}{2}} L_K$. For $Sc_S < 1$, the balance condition is satisfied at a lengthscale above $L_K$, and is of order $L_C = Sc_S^{-\frac{3}{4}} L_K$. Thus, the formal analogy between physical lengthscales and the corresponding model parameters is consistent with the physical criteria determining those lengthscales. In particular, these results show that the formal analogy between $Sc$ and $Sc_S$, where the latter is defined as $(D_T/D_M)/Re_S$, is physically sound. It is noteworthy that the model has a meaningful Schmidt number based on a kinematical analogy, despite the absence of molecular viscosity *per se* in the model.

Having thus derived the balance lengthscales demarcating the various scalar spectral ranges of the model, the functional forms of the spectrum in those ranges are now investigated.

In the inertial-convective range $\max(L_K, L_C) < l \ll L$, molecular diffusion has negligible effect on scalar fluctuations, so the generation and spectral transfer of those fluctuations are governed by the rearrangement process. Fluctuations are generated by each displacement of a fluid element away from the location where its concentration is equal to the local mean value. By virtue of the imposed condition that the diffusivity induced by events of segment-size $l$ or less scale as $l^p$, where $p = \frac{4}{3}$, fluctuations are generated primarily by large-$l$ events, as in real flows. It is assumed that spectral transfer of fluctuation intensity in the inertial-convective range is characterized by a local (in wavenumber) cascade from large to small $l$ that conserves the scalar dissipation. (This is the usual scalar analogue of the Kolmogorov cascade

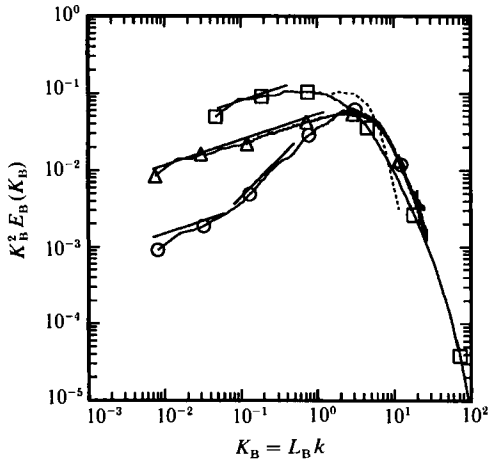


FIGURE 4. Scalar power spectra $E_B$, plotted in a format convenient for identifying scalings, obtained from simulated realizations for $p = \frac{4}{3}$. The subscript B indicates that the model analogue of Batchelor scaling is employed. Namely, the power spectrum is normalized by dividing by $2Re_S^{-\frac{1}{4}}L_B$, where $L_B = Sc_S^{-\frac{1}{2}}Re_S^{-\frac{3}{4}}L$ is the model Batchelor scale. Computed results: △, $Re_S = 10^4$ and $Sc_S = 0.7$; ○, $Re_S = 10^2$ and $Sc_S = 600$; □, $Re_S = 10^4$ and $Sc_S = 0.018$. Also plotted for comparison to scaling predictions are straight line segments of slope $\frac{1}{3}$ (inertial–convective range) and, for $Sc_S = 600$, a line segment of slope 1 (viscous–convective range). The dashed curve, obtained by direct numerical simulation for $Sc = 0.5$ (Kerr 1990), is plotted in model coordinates based on empirical conversions discussed in the text.

of energy dissipation.) In other words, the spectral transfer rate of the squared fluctuation at $l$, which scales as $\delta_l^2/\tau_l$ based on dimensional considerations, is assumed to be independent of $l$ in the inertial-convective range, i.e. $\delta_l^2 \sim \tau_l$. Substituting (8) for $\tau_l$, the result $E \sim l\delta_l^2 \sim l\tau_l \sim l^{3-p} \sim k^{p-3}$ is obtained. In particular, $E \sim k^{-\frac{5}{3}}$ for $p = \frac{4}{3}$.

The assumptions underlying this analysis correspond to the usual (Lesieur 1987) physical picture of the inertial-convective range. The analogy between rearrangement events and eddies is the key to carrying over that physical picture to a modelling approach that does not involve a velocity field.

The $-\frac{5}{3}$ power law governing the scalar spectrum has been confirmed by numerous measurements (Monin & Yaglom 1975). This experimental confirmation does not assure the applicability of the scaling analysis to the present model. To test the scaling analysis, power-law fits to the inertial-convective ranges of simulated scalar power spectra were performed for several $p$ values. Power-law scaling was confirmed, as exemplified by the spectrum for $Sc_S = 0.7$ plotted in figure 4, corresponding to $p = \frac{4}{3}$. (The inertial-convective ranges shown in that figure for other $Sc_S$ values are not well resolved. Various features of figure 4 are discussed shortly.) Deviations of computed exponents from the scaling prediction $p-3$ are shown in figure 5. Although good agreement with the scaling prediction is obtained at $p = \frac{4}{3}$, statistically significant deviations occur at other $p$ values, with a trend that is roughly linear in $p$. These deviations presumably reflect intermittency effects omitted from the scaling analysis.

Since the value $p = \frac{4}{3}$ has no special mathematical significance in the framework of the model, the vanishing of the deviation at or very near $p = \frac{4}{3}$ is apparently fortuitous. Analogous considerations apply to real flows, i.e. theoretical considerations do not rule out deviation from the scaling prediction (Kraichnan 1968), but such deviation is not observed experimentally.

For $Sc_S \gg 1$, there is an additional spectral scaling in the range $l \ll L_K$. For $l \ll L_K$,

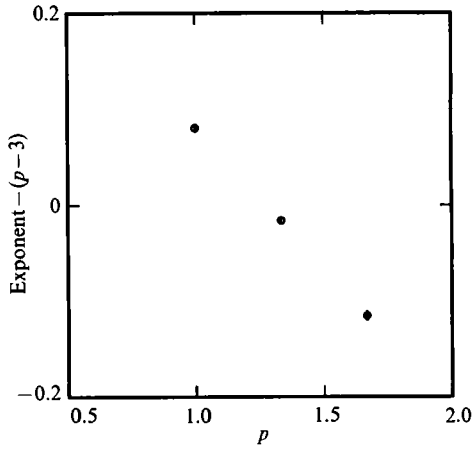


FIGURE 5. Deviation of the computed power-law exponent of the scalar spectrum in the inertial–convective range from the scaling prediction $p-3$, where $p$ is the eddy-diffusivity scaling parameter. ($p = \frac{4}{3}$ corresponds to the Kolmogorov cascade.) Computed exponents are obtained from simulations at $Re_S = 10^4$ and $Sc_S = 0.7$. Error bars (roughly the same size as the symbols) are based on linear fits to log–log plots of computed spectra.

the segment sizes for all rearrangement events are so large relative to $l$ that the effect of a rearrangement on a size-$l$ fluid element may be approximated as a spatially uniform compression. (This approximation is invalid for fluid elements of size $l > L_K$ because entire segments may be contained within fluid elements of size larger than $L_K$.) Fluid elements of size $l \ll L_K$ therefore experience exponential growth of scalar gradients, as discussed in §2, with a characteristic growth rate that is independent of $l$. Kraichnan (1968) has noted that $E(k) \sim k^{-1}$ under these circumstances, provided that other effects such as molecular diffusion are negligible. Since molecular diffusion becomes influential for $l < L_B$, this spectral scaling is limited to the range $L_B < l < L_K$.

The $k^{-1}$ spectrum is a general property of scalar fields, in the model or in real flows, at lengthscales much smaller than those at which the compressive strain is applied. Accordingly, this spectral scaling is obtained experimentally (Monin & Yaglom 1975) and in model computations. A scalar spectrum computed from a simulated realization at $Re_S = 100$ and $Sc_S = 600$ is shown in figure 4. As $k$ increases, the spectrum transitions from the inertial-convective regime (which is poorly resolved due to the low value of $Re_S$) to the $k^{-1}$ scaling, departing from this scaling at high wavenumbers.

The functional form of the high-wavenumber molecular-diffusive cutoff is not firmly established. An analysis that neglects fluctuation effects was performed by Batchelor (1959). He derived the $k^{-1}$ 'viscous–convective' spectral scaling, with an additional multiplicative factor of the form $\exp(-D_M k^2/|\gamma|)$, where $1/|\gamma|$ is a characteristic fluid-mechanical timescale of order $t_K = l_K^2/\nu$. According to his analysis, the exponential cutoff dominates the spectral scaling in the 'viscous–diffusive' range $l \ll l_B$. The effect of fluctuations on the functional form of the cutoff is difficult to analyse systematically. Simplifying assumptions (Kraichnan 1968) yield a falloff of the form $\exp(-k)$, while direct numerical simulation (Kerr 1990) indicates a somewhat slower falloff.

The high-wavenumber properties of the model are impacted by an artifact of the triplet map, namely the discontinuous derivatives of $c(x,t)$ that are introduced. The

spectral manifestation of a discontinuous derivative is a $k^{-4}$ high-wavenumber falloff of the power spectrum. This falloff must be weighted by an amplitude factor reflecting the number density of points of discontinuous derivative in the computational domain. Strictly speaking, their number density is zero because molecular diffusion excises the singularities immediately upon occurrence. However, for given wavenumber $k$, a time interval of order $(k^2 D_M)^{-1}$ is required for molecular diffusion effectively to dissipate the spectral contribution of the singularity at that wavenumber. The measure of the effectively singular region for given $k$ is proportional to $1/k$ times this time interval, yielding a $k^{-3}$ scaling of the amplitude factor, and thus a high-wavenumber scalar power spectrum of the form $E(k) \sim k^{-7}$.

Computed power spectra such as those in figure 4 roll off gradually in the dissipative range, approaching but not reaching the $k^{-7}$ limiting behaviour within the wavenumber range available on the discretized computational domain. Computed spectra, such as that for $Sc_S = 600$ shown in figure 4, exhibit more gradual falloff than spectra obtained by direct numerical simulation (Kerr 1990). (The comparison to Kerr's result is discussed further in §4.2.) This discrepancy may reflect the high-wavenumber spectral input due to the discontinuous derivatives introduced by the triplet map.

For $Sc_S < 1$, molecular diffusion becomes influential at a lengthscale $L_C$ that exceeds $L_K$. For $l < L_C$, the time $t_{mol}(l) \sim l^2/D_M$ for molecular diffusion to dissipate a size-$l$ undulation of the scalar field is less than the characteristic timescale $\tau_l$ governing the generation of undulations by rearrangement events. Since undulations are dissipated more quickly than new undulations appear in this spectral range, they may be viewed as isolated perturbations of a scalar field that is otherwise featureless (i.e. the scalar gradient is roughly constant over a size-$l$ interval). An undulation generated by a size-$l$ event therefore has a typical scalar amplitude $\delta_l \sim gl$, where $g$ is the typical magnitude of the scalar gradient. Based on the balance between generation and molecular dissipation of undulations, the fraction of the spatial domain that is occupied by undulations at any instant scales as $t_{mol}(l)/\tau_l \sim l^{\frac{4}{3}}$, where the exponent reflects the $l$ dependences of the respective timescales. The power spectrum scaling is determined by the spatial integral of the squared scalar amplitude, of order $l\delta_l^2$ times this fraction, giving $E(k) \sim k^{-\frac{13}{3}}$.

The scalar spectrum obtained by simulation for $Sc_S = 0.018$, shown in figure 4, is replotted in figure 6 in a format convenient for identification of the inertial–diffusive scaling. In these figures, the value of the Batchelor-scaled wavenumber $K_B = L_B k$ corresponding to the Batchelor scale is $2\pi$ and the value of $K_B$ corresponding to the Kolmogorov scale is $2\pi L_B/L_K = 2\pi Sc_S^{-\frac{1}{2}} = 47$. Between these nominal limits of the inertial–diffusive range, there is a subrange $10 < K_B < 30$ in which the computed spectrum is roughly consistent with the scaling prediction. (To assess the degree of consistency, note that $K_B^{\frac{13}{3}}$ varies by two orders of magnitude over this subrange.)

Theories and measurements of inertial–diffusive spectral scaling in real low-$Sc$ flows are less definitive than for the other spectral regimes. Batchelor, Howells & Townsend (1959) predicted $k^{-\frac{17}{3}}$ scaling for $L_K < l < L_C$, but Gibson (1968*b*) proposed an alternative $k^{-3}$ scaling. The validity of the latter proposal in the more limited subrange $L_B < l < L_C$ is supported by experimental and computational studies (Clay 1973; Gibson, Ashurst & Kerstein 1988; Kerr 1990). (Those studies also provide evidence, albeit inconclusive, of $k^{-\frac{17}{3}}$ scaling for $L_K < l < L_B$.) The presumed cause of the $k^{-3}$ scaling is the local alignment of the scalar gradient with the compressive strain, resulting in significant gradient amplification over an extended time period. Since convection is implemented as a sequence of instantaneous, statistically

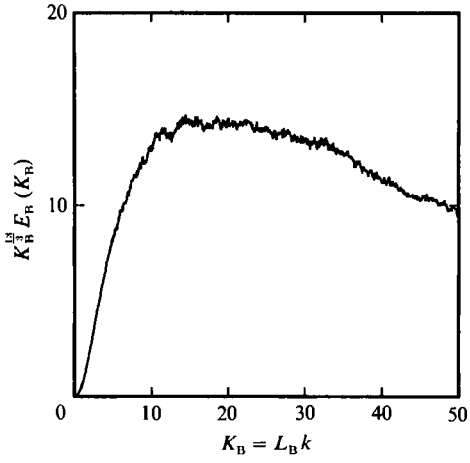


FIGURE 6. Scalar spectrum of figure 4 for $Sc_S = 0.018$, replotted in a format that gives a plateau if $k^{-\frac{13}{3}}$ scaling is obeyed exactly. For this $Sc_S$, the Batchelor scale corresponds to $K_B = 2\pi$ and the Kolmogorov scale corresponds to $K_B = 47$.

independent events in the present formulation, such a mechanism is beyond its scope.

That artifact may also account for the difference between the model inertial–diffusive scaling and the $k^{-\frac{17}{3}}$ prediction of Batchelor *et al.* Based on the timescale inequality $t_{\mathrm{mol}}(l) \ll \tau_l$, Batchelor *et al.* assume an approximate steady-state balance of convective strain and scalar transport. In contrast, undulations are created instantaneously in the present formulation, though molecular dissipation occurs gradually. An aspect common to both derivations is the assumption that high-wavenumber scalar fluctuations are generated by high-wavenumber eddies acting on low-wavenumber scalar variations.

### 4.2. *Spectral amplitudes and transitions*

In the foregoing analysis of spectral scalings, the parameters $Re_S$ and $Sc_S$ determine the wavenumber ranges of the various regimes, but are not involved in the determination of the functional form of the spectral scaling within a given range. Other properties may depend on these parameters, so it is useful to express $Re_S$ and $Sc_S$ in terms of physical quantities. This is done by comparing measured transition wavenumbers and the numerical prefactors of the spectral scalings to their model counterparts.

To perform these comparisons, it is convenient to normalize the spectra in a manner analogous to Batchelor scaling. For measured spectra, Batchelor scaling is obtained by expressing length in terms of $l_B$, time in terms of the Kolmogorov time $t_K = (\nu/\epsilon)^{\frac{1}{2}}$, and scalar amplitude in terms of $(\chi t_K)^{\frac{1}{2}}$, where $\epsilon$ is the mean energy dissipation rate and $\chi$ is the mean scalar dissipation rate (Gibson 1968*b*). Since a measured spectrum $\hat{E}(k)$ has units (scalar amplitude)$^2$ × length, the Batchelor-scaled spectrum $\hat{E}_B(k_B)$ is obtained by dividing $\hat{E}(k)$ by $\chi t_K l_B$ and expressing wavenumber in terms of $k_B = l_B k$. (The hat serves to distinguish measured spectra from spectra obtained from model computations.)

Spectra expressed in model coordinates are scaled in an analogous manner, namely

$$E_B(K_B) \equiv E(K_B)/(\chi T_K L_B), \tag{9}$$

where $K_B = L_B k$ and the model analogue $T_K$ of the Kolmogorov time is taken to be $T_K = Re_S^{-\frac{1}{2}} L^2/D_T$. This expression for $T_K$ is analogous to the inertial-range scaling

property $t_K \sim Re^{-\frac{1}{2}} t_L$. (The model analogue of the large-eddy turnover time $t_L$ is the quantity $T_L = L^2/D_T$ introduced in §2.) It is shown in the Appendix that the mean scalar dissipation rate for the model is $2D_T/L^2$. Based on these relations and the relation $L_B = Sc_S^{-\frac{1}{2}} Re_S^{-\frac{3}{4}} L$, (9) becomes $E_B(K_B) = E(K_B)/(2Sc_S^{-\frac{1}{2}} Re_S^{-\frac{3}{4}} L)$.

The first empirical datum that is introduced is the lengthscale $l^*$ at which high-$Sc$ spectra transition from $k^{-\frac{5}{3}}$ (inertial–convective) to $k^{-1}$ (viscous–convective) scaling. The ratio $l^*/l_K$, where the Kolmogorov scale is empirically defined as $l_K = (\nu^3/\epsilon)^{\frac{1}{4}}$, converges to a constant value in the limit of large $Re$ and large $Sc$. Based on Hill's (1978) analysis of measured spectra, the representative value $l^* = 20 l_K$ is adopted. (Individual measurements depart by as much as 20% from this value.)

The model spectrum of figure 4 for the case $Sc_S = 600$ exhibits the corresponding transition in the vicinity of $K_B = 0.07$. The requirement $K_B = 0.07$ at $l = l^*$ for $Sc_S = 600$, where $K_B = L_B k = 2\pi Sc_S^{-\frac{1}{2}} L_K/l$, gives the result $L_K = 5.5 l_K$, which relates model lengths to physical lengths.

The second empirical datum that is introduced is the amplitude coefficient $\beta$ of the measured spectrum in the inertial–convective range, defined by $\hat{E}(k) = \beta \chi \epsilon^{-\frac{1}{3}} k^{-\frac{5}{3}}$. Based on Hill's (1978) survey of measured spectra, the value $\beta = 0.8$ is representative, with an uncertainty of about 10%. Substituting $\epsilon = \nu^3/l_K^4$, the inertial–convective spectrum becomes $\hat{E}(k) = (\beta\chi/\nu) l_K^{\frac{4}{3}} k^{-\frac{5}{3}}$. Introducing $K_B = L_B k$, dividing by $\chi T_K L_B$, and substituting the definition of $T_K$ and the relation $\nu = D_M Sc$, the result

$$\hat{E}_B(K_B) = \beta \frac{Re_S^{\frac{1}{2}}}{Sc} \left(\frac{l_K}{L_K}\right)^{\frac{4}{3}} \left(\frac{L_B}{L_K}\right)^{\frac{2}{3}} \left(\frac{L_K}{L}\right)^2 \frac{D_T}{D_M} K_B^{-\frac{5}{3}} \tag{10}$$

is obtained. Based on the definitions of $L_B$, $Re_S$ and $Sc_S$, this gives

$$\hat{E}_B(K_B) = \frac{\beta}{Sc_S^{\frac{1}{3}}} \frac{Sc_S}{Sc} \left(\frac{l_K}{L_K}\right)^{\frac{4}{3}} K_B^{-\frac{5}{3}}. \tag{11}$$

For the inertial–convective range model spectrum of figure 4 for the case $Re_S = 10^4$, $Sc_S = 0.7$, a fit of a line of slope $\frac{1}{3}$ to the plotted quantity $K_B^{\frac{2}{3}} E_B(K_B)$ gives

$$K_B^{\frac{5}{3}} E_B(K_B) = 0.047.$$

Setting this equal to $K_B^{\frac{5}{3}} \hat{E}_B(K_B)$ as given by (11) and taking $L_K/l_K = 5.5$ and $\beta = 0.8$ yields $Sc_S = 0.51 Sc$.

Finally, $Re_S = 2.5 Re$ is obtained by inserting this result into the relation $Re_S Sc_S = ReSc/Pr_T$ (which follows from the observation in §2 that both of these quantities are equal to $D_T/D_M$), where the empirical quantity $Pr_T$ is assigned a representative value 0.8. Most measurements of $Pr_T$ are within 20% of this value (Hinze 1975).

Recall that the quantity $Re$ is the local turbulence Reynolds number $\nu_T/\nu$, which need not be the same as a nominal Reynolds number based on the overall flow configuration. Local values of $\nu_T/\nu$ are often unavailable. One robust approach to obtaining a fully quantitative comparison between model results and measurements would be to employ the present formulation as a sub-grid-scale model coupled to a large-eddy or other comparable simulation in which $\nu_T/\nu$ is continually updated locally. This approach would require only the flow geometry and fluid properties as inputs.

With the specification of model parameters in terms of physical quantities thus completed, additional properties of the spectral array of figure 4 are examined. (The 'spectral array' is the family of power spectra parameterized by $Sc$.) First, the $Sc_S$-dependence of the amplitude and the wavenumber range of the inertial–convective regime is considered. The scaling prediction is obtained applying reasoning analogous

to the derivation of (11) to model spectra. This leads to the elimination of all ratios of empirical to model quantities in (11), yielding the prediction that the amplitude should vary as $Sc_S^{-\frac{1}{3}}$ for given $K_B$. Therefore the inertial–convective range of the spectrum of figure 4 for the case $Sc_S = 0.018$ should be parallel to, but a factor $(0.018/0.7)^{-\frac{1}{3}} = 3.4$ above the corresponding range for the case $Sc_S = 0.7$. Similarly, the amplitude ratio 0.11 is obtained for the case $Sc_S = 600$ relative to the case $Sc_S = 0.7$. Figure 4 indicates that the computed spectra obey these relationships despite the fact that the inertial–convective ranges for high and low $Sc_S$ are poorly resolved.

To investigate the low-wavenumber cutoff of the inertial–convective range, a computational domain larger than $L$ would be required. Since the low-wavenumber cutoff is of less interest than the high-wavenumber properties, the computational domain was set equal to $L$ in order to maximize high-wavenumber resolution.

The scaling analysis of §4.1 indicates that the high-wavenumber cutoff of the inertial–convective range occurs at $K_B$ of order $L_B/L_K = Sc_S^{-\frac{1}{2}}$ for $Sc_S$ of order unity or greater. Consistent with this, figure 4 indicates cutoff $K_B$ values in the vicinity of $Sc_S^{-\frac{1}{2}} = 1.2$ and 0.04 for $Sc_S = 0.7$ and $Sc_S = 600$ respectively. (Recall that the inertial-to-convective transition wavenumber was taken to occur at $K_B = 0.07$ for $Sc_S = 600$ based on the computed spectrum.) For $Sc_S \ll 1$, it is shown in §4.1 that the cutoff scale is of order $L_C = Sc_S^{-\frac{1}{4}} L_B$, corresponding to $K_B$ of order $Sc_S^{\frac{1}{4}}$. For $Sc_S = 0.018$, this implies a cutoff in the vicinity of $K_B = 0.37$, consistent with the computed spectrum of figure 4.

Further comparisons require additional explanation of the relationship between physical quantities and the axes of figure 4. To plot a spectrum expressed in the usual Batchelor coordinates (i.e. normalized by $\chi t_K l_B$ and parameterized by $k_B = l_B k$) in terms of the model coordinates according to (9), the following transformation is applied. First, wavenumbers are mapped from $k_B$ to $K_B$ according to $K_B = (L_B/l_B)\, k_B = (Sc_S/Sc)^{-\frac{1}{2}}(L_K/l_K)\, k_B$. Based on the foregoing empirical estimates, this gives $K_B = 7.7 k_B$. Secondly, the Batchelor spectrum is multiplied by $(\chi t_K l_B)/(\chi T_K L_B)$. Substitution of the appropriate definitions and relations reduces this ratio to $(l_B/L_B)^3$. It is especially convenient to plot the quantity $K_B^2 \hat{E}_B(K_B)$. A plot of this quantity in model coordinates is obtained from a Batchelor-scaled plot by multiplying the ordinate by $l_B/L_B$ and dividing the abscissa by the same factor. On a log–log plot, this transformation has the effect of shifting the plotted curve along a line of slope $-1$ without changing its shape. Also, the quantity $\int_0^\infty K_B^2 \hat{E}_B(K_B)\, \mathrm{d}K_B$ is invariant under this transformation. This integral thus has the value $\frac{1}{2}$ in model coordinates as well as in the usual Batchelor coordinates (Gibson 1968*b*). (In fact, the definition of $T_K$ has been chosen so as to preserve this normalization, as explained in the Appendix.) These properties are convenient for distinguishing effects of coordinate scalings from inherent features of the spectrum.

Kerr's (1990) spectrum obtained by direct numerical simulation for the case $Sc = 0.5$ is plotted in this format in figure 4. The spectrum that he obtains for $Sc = 1.0$ collapses to the same curve, and his spectrum for $Sc = 0.1$ deviates only slightly from this curve, with no discernible deviation at high wavenumbers.

Collapse of Batchelor-scaled spectra in the limit of high $Sc$, though not compelled by theory (Kraichnan 1968), follows from the scaling properties presumed to govern the various spectral ranges (Gibson 1968*b*). As $Sc$ decreases below unity, the scalings governing the amplitude and high-wavenumber cutoff of the inertial–convective regime cause the peak of the quantity $K_B^2 E_B(K_B)$ to rise and to shift to lower $K_B$. Since the integral of this quantity is preserved, the high-wavenumber falloff must depart from the high-$Sc$ functional form.

Kerr's results indicate that deviations from high-$Sc$ behaviour become significant only at $Sc$ well below unity. This inference is qualitatively consistent with experimental results concerning a related high-$Sc$ property, the viscous–convective spectral scaling (Hill 1978). (With regard to quantitative consistency, note that a line of slope unity projected downward from the leftmost point of Kerr's spectrum does not merge with the viscous–convective range of the model spectrum for $Sc_S = 600$. This discrepancy reflects the inexactness of the empirical inputs, since amplitudes and cutoffs of model spectra have been referenced to their measured counterparts.)

The upshot of these observations is that dissipation-range collapse should be exhibited only by spectra whose inertial–convective ranges meet the high-$Sc$ 'universal curve' at a point well to the left of the peak of $K_B^2 E_B(K_B)$. As discussed in §4.1, model spectra roll off more gradually than Kerr's spectra in the dissipation range, so the area normalization requires high-$Sc$ model spectra to exhibit lower peaks than Kerr's spectra. Therefore, dissipation-range collapse of model spectra does not extend to $Sc$ as low as for spectra from Kerr's simulations.

Apart from this discrepancy and aspects of inertial-diffusive scaling discussed in §4.1, the model spectra of figure 4 agree with the trends and features of the spectral array as summarized by Gibson (1968*b*). (Compare the Batchelor-scaled spectral array shown in figure 4 of that reference.) This comparison supports the analogies that relate model parameters to physical quantities. It is noteworthy that these analogies lead to a comprehensive description of scalar mixing that does not involve dynamical quantities such as $\epsilon$ and $\nu$. It is not surprising that this can be achieved, because scalar mixing is governed solely by the kinematics of the flow field, so a model need only capture the relevant kinematics in order to characterize mixing properly. It is perhaps more surprising that the spectral array is well characterized by a formulation based on instantaneous rearrangements rather than continuum flow. In the Appendix, some of the standard relationships governing transport and mixing are rederived in a generalized framework in order to demonstrate that many intuitive notions based on continuum flow remain valid in the present context.

## 5. Intermittency

Some model properties considered thus far are sensitive to fluctuations resulting from the stochastic nature of the rearrangement process. Features of the scalar dissipation p.d.f. and deviations of certain spectral scaling exponents from estimated values have been interpreted as manifestations of such intermittency effects.

The most significant manifestations of intermittency are the scaling properties of quantities that are highly sensitive to extreme fluctuations of the scalar field. Two families of scaling exponents that are sensitive to extreme fluctuations have been studied extensively, the generalized dimensions $D_q$ and the structure–function exponents $\zeta'_n$. To investigate the intermittency properties of the model, these exponents are determined from simulated realizations by procedures similar to those applied to measurements of the scalar field along a line.

It has been proposed on the basis of scale similarity that the average $\chi_r$ of the scalar dissipation rate over a zone of size $r$ should exhibit scaling of the form $\langle(\chi_r/\chi_L)^q\rangle \sim (L/r)^{\mu'_q}$ in the inertial–convective range (Monin & Yaglom 1975). (Primes on scaling exponents serve to distinguish them from exponents governing energy-dissipation intermittency.) This scaling has been confirmed experimentally (Antonia & Sreenivasan 1977). In more recent work, the scaling exponents have been reparameterized in terms of a family of generalized dimensions $D_q = 3 - \mu'_q/(q-1)$

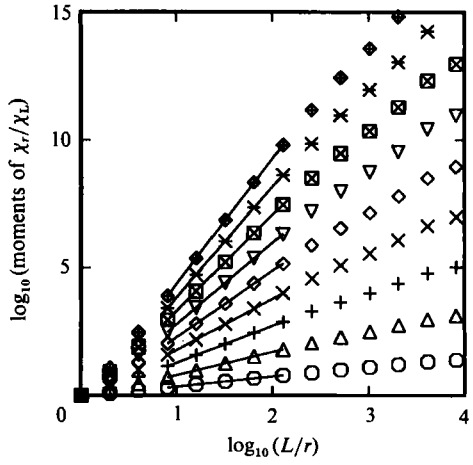


FIGURE 7. Log–log plot of $\langle(\chi_r/\chi_L)^q\rangle$ versus $L/r$, where $\chi_r$ is the average of the scalar dissipation rate over a size-$r$ interval, computed for $Re_S = 10^4$ and $Sc_S = 0.7$. For given $r$, the plotted quantity increases with increasing $q$, with the respective symbols denoting $q = 2$–10. The slopes of the fitted straight-line segments are the inferred values of the scaling exponents $\mu'_q$.

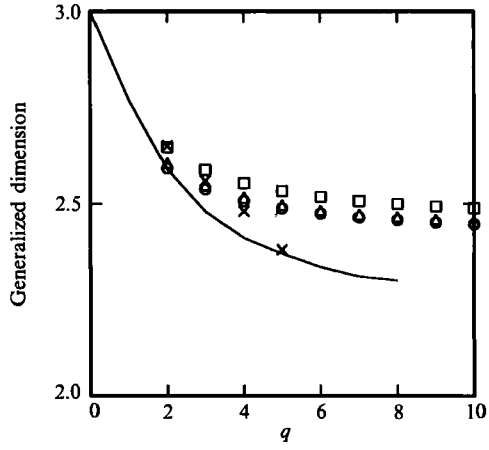


FIGURE 8. Generalized dimensions $D_q$ computed in the inertial-convective range for $Re_S = 10^4$ and $Sc_S = 0.7$: ○, $p = 1$; △, $p = \frac{4}{3}$; □, $p = \frac{5}{3}$; measured: ——, Sreenivasan & Prasad 1989; ×, Antonia & Sreenivasan 1977.

that can be transformed to obtain the multifractal spectrum of the dissipation field (Prasad, Meneveau & Sreenivasan 1988). Computed results are reported here in terms of $D_q$ to facilitate comparison to recent measurements (Sreenivasan & Prasad 1989).

Figure 7 illustrates the determination of the exponents $\mu'_q$ from simulations by a method like that of Sreenivasan & Prasad. Power-law scaling is obtained because the requisite scale similarity is built into the model. Computed and measured $D_q$ values are plotted in figure 8.

Statistics were gathered for 10 large-eddy turnover times (defined in §2) for the cases $p = \frac{4}{3}$ and $p = \frac{5}{3}$, but for only one large-eddy turnover time for $p = 1$ owing to the high computational cost of that case. Since $p = \frac{4}{3}$ corresponds to the Kolmogorov eddy-size distribution, it is the case comparable to measurements.

In view of the potential sensitivity of large-$q$ statistics to computational artifacts, several runs were performed for $p = \frac{4}{3}$ involving variations of spatial resolution, time-

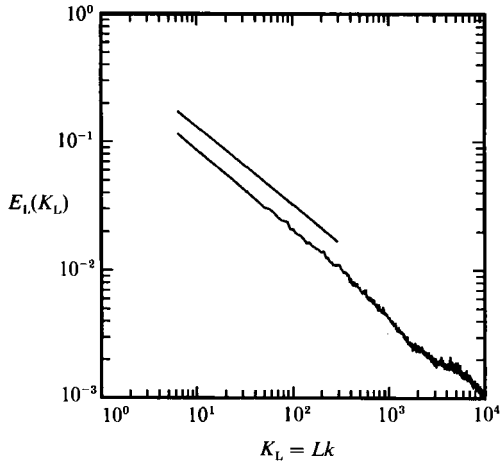


FIGURE 9. Power spectrum $E_L$ of the scalar dissipation rate, computed for $Re_S = 10^4$ and $Sc_S = 0.7$. (The subscript denotes normalization by $\chi^2 L$, where $\chi$ is the mean scalar dissipation rate.) A line segment of slope $\mu_2' - 1 = 2 - D_2 = -0.606$ is plotted for comparison. (The numerical value is based on the $q = 2$ fit of figure 7.)

step, $Re_S$, and the random-number seed. These variations had only a slight effect on the results, indicating that the $p$ sensitivity evident in figure 8 is a property of the model rather than a computational artifact. Another sensitivity test involved adoption of the quintuplet map defined in §2 instead of the triplet map. For $p = \frac{4}{3}$, the $D_q$ values based on the quintuplet map were found to be consistently lower than those based on the triplet map by about 0.05, indicating that the results are not very sensitive to the choice of mapping rule.

It is not evident whether the differences between the results for the case $p = \frac{4}{3}$ and measured values are statistically significant, because measurement precision was not reported. Precision is impacted both by spatial differentiation of the scalar field and by taking high moments of the differentiated field. Comparison of the two sets of measurements plotted in figure 8 to infer precision may be misleading because large-$q$ results are the least reliable, but the measurements are in best agreement at the largest $q$ value for which a comparison is available. In any event, it is evident that model results are in rough, if not exact, agreement with measurements.

Computed $D_q$ values for negative $q$ (not shown) are much larger than measured values. For negative $q$, $D_q$ is sensitive to incipient singularities of the inverse of the scalar dissipation, i.e. to zones of low dissipation. As discussed at the end of §2, zones of low dissipation are disproportionately weighted in the model because the computational domain is effectively a space curve locally aligned with the scalar gradient. As emphasized in that discussion, the model provides a better representation of the 'active' (high-dissipation) than of the 'passive' (low-dissipation) zones of the scalar field.

Scale similarity implies that the scalar intermittency exponent $\mu_\theta$, defined by the relation $\langle \chi(x)\chi(x+r)\rangle \sim r^{-\mu_\theta}$ in the inertial–convective range, is identical to $\mu_2'$ (Monin & Yaglom 1975). Therefore the power spectrum of scalar dissipation should scale as $k^{\mu_2'-1}$ in the inertial–convective range. The model exhibits this scaling, as indicated by the computed power spectrum plotted in figure 9.

The scalar structure function of order $n$ is defined as $\langle [c'(x,t) - c'(x+r,t)]^n \rangle$. Scale similarity implies $\langle [c'(x,t) - c'(x+r,t)]^n \rangle \sim r^{\zeta_n}$ (Van Atta 1971).

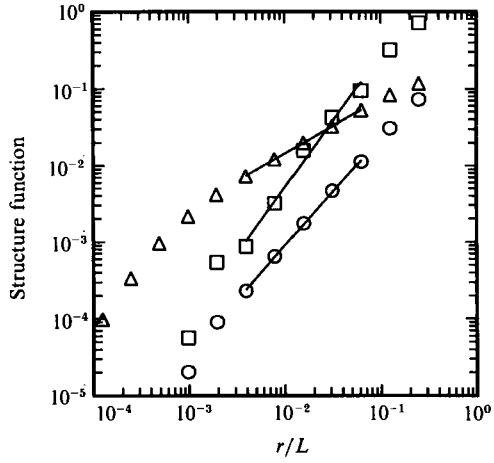


FIGURE 10. Log–log plot of the order-$n$ scalar structure function $\langle[c'(x,t)-c'(x+r,t)]^n\rangle$ versus $r/L$, computed for $Re_S = 10^4$ and $Sc_S = 0.7$: △, $n = 2$; ○, $n = 8$; □, $n = 14$. The slopes of the fitted straight-line segments are the inferred values of the scalar structure-function exponents $\zeta'_n$.

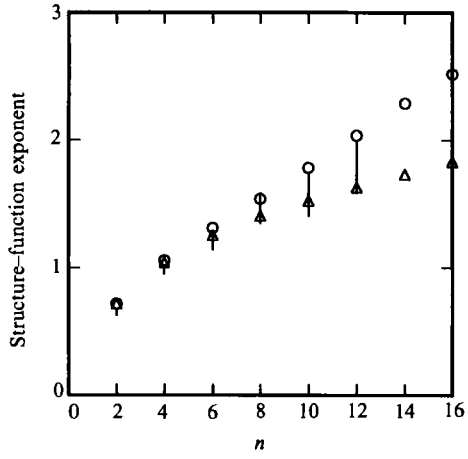


FIGURE 11. Scalar structure-function exponents $\zeta'_n$ computed in the inertial–convective range for $Re_S = 10^4$ and $Sc_S = 0.7$: △, base case; ○, replicate based on a different random-number seed. For $2 \leqslant n \leqslant 6$, vertical line segments span the range of reported point measurements compiled by Antonia *et al.* (1984). For $8 \leqslant n \leqslant 12$, vertical line segments are error bars reported by Antonia *et al.* (1984) based on their measurements.

Figure 10 illustrates the determination of the scalar structure–function exponents $\zeta'_n$ from simulations. Compared to figure 7 for the generalized dimensions, the scaling range is narrower and statistical fluctuations are larger. Computed and measured $\zeta'_n$ values are plotted in figures 11 and 12. As a baseline for comparison, note that $\zeta'_n = \frac{1}{3}n$ if intermittency effects are absent, i.e. if fluctuation statistics are purely Gaussian (Van Atta 1971).

Runs performed for $p = \frac{4}{3}$ involving variations of spatial resolution, timestep and $Re_S$ indicate at most a slight sensitivity to these variations. The effect of changing the random-number seed is more significant, as shown in figure 11. Longer run times could improve the statistical precision. The precision indicated by figure 11 is sufficient for present purposes, since it is comparable to experimental precision. It is evident that model results and measurements are in satisfactory agreement. More

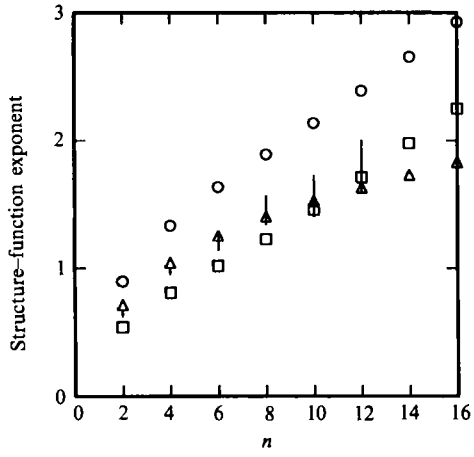


FIGURE 12. Scalar structure-function exponents $\zeta'_n$ computed in the inertial–convective range for $Re_S = 10^4$ and $Sc_S = 0.7$: ○, $p = 1$; △, $p = \frac{4}{3}$ (base case of figure 11); □, $p = \frac{5}{3}$. Measurements as in figure 11.

precise measurements and longer computational run times would provide a more stringent test of that agreement at large $n$.

Comparison of figures 11 and 12 indicates that the $p$ sensitivity of the computed results is statistically significant. Satisfactory agreement with all measured $\zeta'_n$ values is obtained only for the value $p = \frac{4}{3}$ corresponding to the Kolmogorov eddy-size distribution. This supports the contention that the eddy ensemble generated by the model is physically meaningful, because it reproduces the measured fluctuation statistics only when the physically correct eddy-size scaling is adopted.

The set of exponents $\zeta'_n$ for $p = \frac{4}{3}$ was also computed from simulations using the quintuplet map instead of the triplet map. For each $n$ value, it is found that the result based on the quintuplet map falls between the pairs of computed triplet-map values shown in figure 11, indicating that these results as well as the results for $D_q$ are not very sensitive to the choice of mapping rule.

The favourable comparisons between computed and measured scalar intermittency statistics are particularly noteworthy in the context of intermittency models proposed to date. Previous models have achieved good agreement with measurements only through the incorporation of empirical inputs or adjustable parameters (Andrews & Shivamoggi 1990). The only quantitative input required in the present model is the exponent $p$ governing the relation between eddy size and diffusivity, whose value $\frac{4}{3}$ follows from dimensional analysis based on the Kolmogorov picture of the inertial-range cascade. The results are sensitive to $p$ but not to the mapping rule chosen to represent individual eddies. As in §4.1, the parameters $Re_S$ and $Sc_S$ serve to demarcate the scaling regime but do not determine scaling exponents, which are asymptotic properties of the limit $Re_S \to \infty$.

The aspect of the model that determines its intermittency characteristics is the random process governing the sequence of rearrangement events. Here, the simplest possible assumption concerning this process has been adopted. Namely, it has been assumed that the locations and epochs of individual events are statistically independent, so that the sequence of events constitutes a Poisson process in space and time. The good agreement with measurements lends support to the proposal (Andrews *et al.* 1989) that Poisson statistics may provide a sound basis for modelling intermittency.

## 6. Fractal dimension of scalar isopleths

Many geometric properties of an isopleth (constant-property surface) in an isotropic concentration field are directly related to properties of the set of points comprising the intersection of the isopleth with a straight line. In particular, the fractal dimension $D_f$ of concentration isopleths in turbulence has been estimated from line measurements by applying the 'additive law', which states that the isopleth fractal dimension in $d$-dimensional space is $n$ plus the fractal dimension of the intersection of the isopleth with a $(d-n)$-dimensional manifold (Prasad & Sreenivasan 1990). For the case considered here, $d = 3$ and $n = 2$. In view of this relationship, one can determine $D_f$ for the isopleth by determining $D_f$ for its intersection with a line. $D_f$ for the line intersection is considered here because the set of points comprising the intersection is analogous to level sets of simulated realizations of $c(x,t)$.

It is not immediately evident whether level sets of the scalar field $c(x,t)$ or of the mean-subtracted scalar field $c'(x,t)$ are more directly analogous to measured level sets. To identify the qualitative distinction between these level sets, note that each level set of $c'(x,t)$ is a homogeneous random process on the spatial domain, and that excursions of $c'(x,t)$ to levels far exceeding $\langle c'^2\rangle^{\frac{1}{2}}$ are rare. The latter property indicates that the level sets of $c'(x,t)$ are not all statistically equivalent. In contrast, each level set of $c(x,t)$ is contained within a finite interval of the spatial domain, typically of order $L$. The initial and boundary conditions assure that all level sets of $c(x,t)$ are statistically equivalent. The term 'level invariance' is adopted to denote this property.

The properties of spatial homogeneity and level invariance are mutually incompatible not only in the present modelling framework, but for any scalar field with finite $\langle c'^2\rangle$. In fact, experimental configurations can satisfy either property at best over a limited spatial extent or over a limited range of concentration levels. It would therefore appear that neither type of level set can be unequivocally identified as the model analogue of measured level sets.

This ambiguity is of practical relevance because model computations indicate that the two types of level sets exhibit qualitatively different geometric properties. (The cases considered, methods of data reduction, and detailed results are presented in Kerstein 1991*b*. Here, the results are briefly summarized.) Level sets of $c(x,t)$ exhibit fractal scaling with $D_f = 0.44$ for the triplet map and $D_f = 0.41$ for the quintuplet map. (Scaling analysis applied to the model yields the estimate $D_f = \frac{1}{3}$, identical to the scaling prediction for real flows (Sreenivasan *et al.* 1989). Deviations from the scaling estimate reflect intermittency effects.) Level sets of $c'(x,t)$ do not exhibit fractal scaling, but can be characterized using the 'local dimension' defined by Miller & Dimotakis (1991).

Experimental observations of fractal scaling in a variety of turbulent flows are summarized by Prasad & Sreenivasan (1990), who conclude that $D_f = 0.36 \pm 0.05$. The deviation of this value from the scaling prediction $D_f = \frac{1}{3}$, though perhaps not statistically significant, is consistent with a modified scaling analysis that accounts for local fluctuations of flow-field properties (Meneveau & Sreenivasan 1990). Other measurements (Miller & Dimotakis 1991) indicate the absence of fractal scaling. Comparisons of the latter measurements to model results in terms of local dimension are presented elsewhere (Kerstein 1991*b*). There it is proposed that the conceptual distinction between the two types of level sets may manifest itself experimentally through subtle differences among measurement techniques or flow conditions.

Here and in §5, the quintuplet map has been found to yield comparable or slightly better agreement with measurements than does the triplet map. The improvement is not large enough to indicate a preference for the quintuplet map, in view of the intuitive appeal of the triplet map as a representation of a single eddy (figure 2). However, it is interesting to note that the quintuplet map or higher '$n$-tuplets' may have some mechanistic basis if postulated helical or related structures become recognized as the canonical structures of turbulent eddies.

## 7. Lagrangian analysis

Since the present modelling approach involves simulation of time-histories of a self-contained computational domain (rather than a fixed control volume imbedded in a flow), the model can be interpreted from a Lagrangian as well as an Eulerian viewpoint. To illustrate the Lagrangian interpretation, the dispersion of a spot of scalar contaminant is considered, yielding the model analogue of Richardson's dispersion law (Monin & Yaglom 1975).

Regard the spot as infinitesimal initially. After an elapsed time $t$, the spot size $s$ has increased to a finite value owing to molecular diffusion and rearrangements. For $t \ll T_K$, where $T_K$ is defined below (9), the spot is affected only by molecular diffusion, so $s^2$ is of order $D_M t$. Beginning at $t$ of order $T_K$, the spot also grows owing to rearrangements. A size-$l$ event containing some or all of the spot creates three images distributed over a region of order $l$, resulting in a spot size $s$ of order $l$ (or possibly greater, if the spot size prior to the event exceeds $l$). Thus, $s$ is at least of order $l(t)$, where $l(t)$ is the size of the largest mapping that intersects the spot during $[0, t]$. (For $t < T_L$, $s$ is no larger than order $l(t)$ because there is no other dispersion mechanism to make it larger.)

Note that $s$ may greatly exceed the total measure of the zones in which 'significant' contaminant concentrations (based on any convenient criterion) are found. This reflects the streakiness of the scalar, i.e. the tendency of the stirring process to form thin ribbons of contaminant separated by essentially contaminant-free regions (Garrett 1983).

The $t$ dependence obtained for $s(t)$ depends on whether the 'typical' (most probable) or the root-mean-square value of $s(t)$ is considered. The typical value is of the order of the size of the largest event whose characteristic time $\tau_l$ is of order $t$ or less. According to (8), this implies $s(t) \sim t^{1/(2-p)}$ for $T_K < t < T_L$. Specializing to $p = \frac{4}{3}$, this implies $s(t) \sim t^{\frac{3}{2}}$. This scaling can be expressed in the form $ds^2/dt \sim D_T(s)$, where the effective diffusivity $D_T(s)$ governing the dispersion process scales as $s^{\frac{4}{3}}$. The Richardson law is thus recovered.

The mean-square spot size $\langle s^2(t) \rangle$ scales in the same manner as the mean-square Eulerian displacement of a passive marker because a size-$l$ event has an order-$l$ effect in both cases, irrespective of the magnitude of $l$. (An eddy of size $l \gg s$ in a real flow induces an order-$l$ Eulerian displacement, but has less effect on $s$.) As shown in the Appendix, the Eulerian displacement increases diffusively with diffusivity $D_T$ for all $t$. This gives $\langle s^2(t) \rangle \sim t$, in disagreement with the Richardson law. Likewise, the Eulerian result disagrees with theoretical (Taylor 1921) and experimental (Warhaft 1984) results indicating that the mean-square Eulerian displacement is proportional to $t^2$ in the regime $T_K < t < T_L$. The latter scaling is a consequence of the constant-velocity displacement induced by a size-$L$ eddy over that time interval. This mechanism is not captured by the present formulation because rearrangement events are instantaneous.

These considerations indicate that the applicability of the model to transient dispersion may depend on the precise question that is addressed.

## 8. Discussion

The linear-eddy modelling approach is shown here to provide an economical, physically sound characterization of turbulent mixing based on a one-dimensional stochastic process that emulates higher-dimensional convective stirring mechanisms, with sufficient spatial resolution to allow direct, concurrent implementation of molecular diffusion. This direct implementation of molecular diffusion in Monte Carlo simulations of individual mixing-field realizations is the key to obtaining computed *Sc* dependences consistent with physical intuition and experimental results.

A feature common to both the present and previous formulations is the representation of convective stirring by a rearrangement process consisting of a sequence of instantaneous, statistically independent mapping events. In the present formulation, the mapping rule that is adopted is the 'triplet map' (and in some cases, a variant denoted the 'quintuplet map'), advantageous because it emulates the multiplicative increase of scalar gradients that is induced by compressive strain. It has also been noted that the effect of a single mapping event on the scalar field is analogous to the effect of an eddy of corresponding size.

Previous applications of the linear-eddy approach addressed single-point statistics of the mixing field. A study of mixing-field microstructure, characterized primarily by multipoint statistics such as power spectra, is reported here. Model computations are found to reproduce key features of measured scalar power spectra, parameterized by *Re* and *Sc*, and to yield numerical values of scaling exponents governing higher-order fluctuation statistics that are close to measured values. Other aspects of microstructure that are examined include the probability distribution of the scalar dissipation rate and the fractal dimension of level sets.

To place these results in perspective, it should be noted that the only numerical input needed to obtain the aforementioned results is an exponent governing the size distribution of mapping events. This exponent is determined from dimensional considerations as prescribed by the Kolmogorov cascade picture of inertial-range turbulence. Thus, the qualitative and quantitative agreement that is obtained does not rely on any empirical inputs or adjustable parameters.

Spectral scaling properties of the model are interpreted on the basis of scaling analysis analogous to the usual reasoning. The agreement with the principal features of the measured spectral array appears to be a consequence of (i) the explicit incorporation of inertial-range scaling, (ii) a physically sound representation of the viscous range achieved by formulating a mapping rule that emulates compressive strain, and (iii) direct implementation of molecular diffusion. Therefore the spectral results are not very surprising, though they are important indicators of the soundness of the model.

In contrast, there is no reason to assume that the model embodies the correct fluctuation properties determining higher-order scaling exponents such as scalar structure–function exponents. It is therefore noteworthy that the model yields numerical values close to measured results. In particular, it is noteworthy that the agreement is better when the size distribution of maps is specified in accordance with the Kolmogorov inertial-range scaling than when other, arbitrary scalings are chosen. These results suggest that the eddy concept, whose model analogue is the

individual mapping event, has some quantitative validity not only as a picture of typical behaviour, but also as a picture of instantaneous deviations from typical behaviour. (This proposal is also supported by a recent analysis of velocity fluctuations in turbulence (She & Orszag 1991).) In particular, the present results indicate that the postulated statistical independence ('Poisson ensemble') of mapping events is a reasonable working hypothesis, consistent with an earlier proposal (Andrews *et al.* 1989).

The scaling properties associated with the statistical ensemble are also of interest from the viewpoint of chaos induced by iterated nonlinear maps. Deterministic iteration of two-dimensional nonlinear maps that emulate scalar-gradient amplification by compressive strain has been shown to generate chaotic scalar fields exhibiting multifractal scaling (Ott & Antonsen 1989). The values of the generalized dimensions $D_q$ characterizing this scaling are model-dependent. It was suggested that extension to turbulent mixing might require randomization of the ensemble of maps. This suggestion is implemented, in effect, in the present one-dimensional formulation.

In this regard, it is noteworthy that non-trivial fractal and multifractal scalings and related intermittency properties arise in the present formulation as a consequence of the specified size distribution of maps, with no fractal interdependence (in fact, no interdependence whatsoever) among the spatial locations of mapping events. This result is consistent with the finding of Kraichnan (1990) that many fluctuation properties of turbulence can be explained without recourse to a fractal causative process.

The present work can also be viewed from the perspective of efforts to develop robust computational procedures applicable to complicated mixing flows. Although the present formulation, supplemented by configuration-specific empiricism, can address issues of practical importance (Kerstein 1988, 1989, 1990, 1991*a*), its greatest potential utility is as a subgrid mixing model coupled to a large-eddy or other comparable simulation. The model is readily adapted to this application by relating the linear-eddy nominal Reynolds number $Re_S$ to the large-eddy cell Reynolds number, and implementing a linear-eddy simulation within each large-eddy cell. Alternatively, the large-eddy-simulated flow field may convect Lagrangian fluid particles, each of which has an internal structure that evolves according to a linear-eddy simulation. Rules determining the exchange of species between nearby fluid particles would be needed, as in other subgrid mixing models. The empirical relations of §4.2, expressing model parameters in terms of physical quantities, provide a basis for quantitatively accurate coupling of the subgrid model to the large-eddy simulation.

Such a formulation would be compatible with massively parallel computation because a linear-eddy subgrid model would involve greater temporal as well as spatial resolution than a large-eddy simulation. Therefore processors implementing individual linear-eddy simulations would compute for many timesteps between communications with other processors.

The model is subject to several artifacts whose impact on predicted mixing-field microstructure has been identified. First, the representation of eddies by instantaneous events rather than by processes of finite time duration causes discrepancies in the exponents governing the inertial–diffusive spectral scaling and certain transient dispersion scalings. Secondly, implementation of the model in one spatial dimension simulates, in effect, the scalar field along a time-varying space curve locally aligned with the scalar gradient. As explained in §2, this causes excessive creation of zero-gradient points, impacting properties sensitive to the

prevalence of low-gradient regions. Thirdly, discontinuous derivatives introduced by the mapping process cause excessive high-wavenumber spectral input, possibly explaining the slower-than-observed high-wavenumber spectral falloff.

Despite these limitations, it is evident that the present formulation captures many key features of turbulent mixing. The scope of the approach, encompassing single-point scalar properties, spectral and higher-order multipoint scaling properties, fractal geometry and Lagrangian scalings, provides a unified treatment of a variety of phenomena usually addressed using disparate models whose mutual compatibility is not self-evident. The demonstration here that all these properties are captured within a simple modelling framework is compelling evidence that these properties can be viewed as various manifestations of a single postulated scaling property (inertial-range self-similarity) of high-Reynolds-number turbulence.

The author would like to thank Paul Dimotakis and Eric Siggia for helpful discussions. This research was supported by the Division of Engineering and Geosciences, Office of Basic Energy Sciences, US Department of Energy.

## Appendix. Analysis of transport and mixing

Expressions are derived that relate the model turbulent diffusivity to other model parameters and to physical quantities. Some of the expressions are formally identical to standard results governing turbulent mixing. The derivations presented here serve to formalize the analogy between model parameters and physical quantities. In particular, the analogy between the model scalar power spectrum and the measured spectrum is formalized.

Consider first the diffusion coefficient $D_T$ governing the random walk of an infinitesimal fluid element. The total mean-square displacement induced by statistically independent rearrangement events during a time interval $t$ is

$$\langle(\Delta x)^2\rangle = \left\langle\left(\sum_{j=1}^{N}\delta_j\right)^2\right\rangle = \langle N\rangle\langle\delta^2\rangle, \tag{A 1}$$

where $\delta_j$ is an individual displacement and the random variable $N$ is the number of displacements of the fluid during a time interval $t$. The right-hand expression, in which $\langle\delta^2\rangle$ denotes the mean-square displacement induced by a single event, follows from the assumptions that individual displacements are statistically independent with respect to magnitude as well as time of occurrence, and that the mean individual displacement is zero. (The latter property is a consequence of spatial homogeneity.)

The size-$l$ mappings that can displace a given fluid element are those whose centres fall within a distance $\frac{1}{2}l$ from the fluid element, i.e. within an interval of size $l$ centred at the fluid element. Based on the definitions of $\lambda$ and $f(l)$, the frequency of displacements induced by eddies in the size range $[l, l+\mathrm{d}l]$ is $\lambda l f(l)\,\mathrm{d}l$. Therefore $\langle N\rangle = Rt$, where $R = \lambda\int lf(l)\,\mathrm{d}l$ is the total frequency of displacements. Let $\langle\delta^2(l)\rangle$ be the mean-square displacement induced by one size-$l$ mapping. Then $\langle\delta^2\rangle$ is the frequency-weighted average of $\langle\delta^2(l)\rangle$, namely

$$\langle\delta^2\rangle = R^{-1}\lambda\int lf(l)\langle\delta^2(l)\rangle\,\mathrm{d}l. \tag{A 2}$$

$\langle\delta^2(l)\rangle$ is evaluated by expressing it as $\langle\delta^2(l)\rangle = l^{-1}\int_{-l/2}^{l/2}\delta^2(l\,|\,z)\,\mathrm{d}z$, where $\delta^2(l\,|\,z)$ is the square of the displacement given that, after displacement, the fluid element is a distance $z$ from the centre of the size-$l$ segment causing the displacement. (This expression is based on the uniform distribution of $z$ over $[-\frac{1}{2}l, \frac{1}{2}l]$. It is convenient but

not essential to condition on the relative location after rather than before displacement. This avoids explicit consideration of the three post-images of each fluid-element pre-image.) For the triplet map, it follows from (2) that

$$\delta^2(l\,|\,z) = \begin{cases} 16z^2 & 0 \leqslant |z| \leqslant \frac{1}{6}l \\ (l-2|z|)^2 & \frac{1}{6}l \leqslant |z| \leqslant \frac{1}{2}l. \end{cases} \tag{A 3}$$

Substitution of (A 3) into the expression for $\langle\delta^2(l)\rangle$ gives $\langle\delta^2(l)\rangle = \frac{4}{27}l^2$. Based on this result, (A 1) and (A 2), and the relation (Hinze 1975)

$$D_{\mathrm{T}} = \langle(\Delta x)^2\rangle/(2t), \tag{A 4}$$

(3) of §2 is obtained.

Next, the model analogue of a standard expression for the mean scalar dissipation rate $\hat{\chi}$ is derived. (Here, physical quantities are denoted by hats where needed to distinguish them from model parameters.) Tennekes & Lumley (1972) show that the balance equation for the mean-subtracted scalar $c'$ reduces to

$$-\langle c'\boldsymbol{u}\rangle\cdot\boldsymbol{\nabla}\Theta = \hat{D}_{\mathrm{M}}\langle(\boldsymbol{\nabla}c')^2\rangle \equiv \tfrac{1}{2}\hat{\chi} \tag{A 5}$$

in steady homogeneous flow, where $\boldsymbol{u}$ is the fluid velocity referenced to the mean flow, $\boldsymbol{\nabla}\Theta \equiv \langle\boldsymbol{\nabla}c\rangle$ is the imposed scalar gradient, and the right-hand equality is one of several equivalent defining relations for $\hat{\chi}$ that appear in the literature. (A non-equivalent definition is also prevalent, differing from (A 5) by a factor of 2. Here, the conventions adopted by Batchelor (1959) are followed.) The turbulent diffusivity $\hat{D}_{\mathrm{T}}$ is operationally defined as the coefficient relating the imposed scalar gradient to the flux of $c'$ according to the Fourier law $\langle c'\boldsymbol{u}\rangle = -\hat{D}_{\mathrm{T}}\boldsymbol{\nabla}\Theta$ (Hinze 1975). In conjunction with (A 5), this gives

$$\hat{\chi} = 2\hat{D}_{\mathrm{T}}(\boldsymbol{\nabla}\Theta)^2. \tag{A 6}$$

The model parameter $\chi$ is defined as $2D_{\mathrm{M}}\langle(\boldsymbol{\nabla}c')^2\rangle$ based on the discussion in §2. To establish the analogy between physical quantities and the corresponding model parameters $D_{\mathrm{M}}$, $D_{\mathrm{T}}$ and $\chi$, it must be shown that the model obeys the analogue of (A 6), namely $\chi = 2D_{\mathrm{T}}(\boldsymbol{\nabla}\Theta)^2$. This result is derived by considering the time evolution of the mean-subtracted scalar $c'$ associated with a given fluid element. Denote the scalar value within the fluid element as $c$ at time $t$ and $c+\Delta c$ at time $t+\Delta t$, where $\Delta t$ is small. Likewise, denote the location of the fluid element as $x$ and $x+\Delta x$ at the respective times. Owing to the non-local character of mapping events, $\Delta x$ is not small in each realization, but its mean-square value, governed by (A 4), is of order $\Delta t$. In this notation, $c'(t) = c - x/L$ and $c'(t+\Delta t) = c+\Delta c-(x+\Delta x)/L$ for the initial-value problem formulated in §2. Squaring the latter quantity, ensemble averaging, and taking $\langle c'^2(t+\Delta t)\rangle = \langle c'^2(t)\rangle$ owing to statistical stationarity, the result

$$\langle(\Delta c)^2\rangle + \langle(\Delta x)^2\rangle/L^2 - 2\langle\Delta c\,\Delta x\rangle/L + 2\langle c'(t)\Delta c\rangle - 2\langle c'(t)\,\Delta x\rangle/L = 0 \tag{A 7}$$

is obtained.

The individual terms of (A 7) are evaluated as follows. Since $c$ within a fluid element changes only by molecular diffusion,

$$\Delta c = D_{\mathrm{M}}(\nabla^2 c)\,\Delta t = D_{\mathrm{M}}(\nabla^2 c')\,\Delta t. \tag{A 8}$$

Therefore $\langle(\Delta c)^2\rangle$ is of order $(\Delta t)^2$, which is negligible compared to other terms. $\langle(\Delta x)^2\rangle$ is evaluated by applying (A 4), which gives $\langle(\Delta x)^2\rangle = 2D_{\mathrm{T}}\,\Delta t$.

Equation (A 8) indicates that $\Delta c$ is of order $\Delta t$. In the limit of small $\Delta t$, the probability of non-zero $\Delta x$ is proportional to $\Delta t$. Therefore $\langle\Delta c\,\Delta x\rangle$ is of order $(\Delta t)^2$.

According to (A 8), $\langle c'(t)\,\Delta c\rangle = D_{\mathrm{M}}\,\Delta t\langle c'(t)\,\nabla^2 c'\rangle$. The familiar (Batchelor 1959) relation $\langle c'(t)\,\nabla^2 c'\rangle = -\langle(\nabla c')^2\rangle$ follows from the identity $\nabla\cdot(c'\nabla c') = c'\nabla^2 c' + (\nabla c')^2$ by noting that the expectation value of the left-hand side of that identity vanishes owing to the spatial homogeneity of $c'$. Therefore

$$2\langle c'(t)\,\Delta c\rangle = -2D_{\mathrm{M}}\,\Delta t\langle(\nabla c')^2\rangle \equiv -\chi\Delta t.$$

Finally, the statistical independence of rearrangement events implies $\langle c'(t)\,\Delta x\rangle = \langle c'(t)\rangle\langle\Delta x\rangle$. Both terms in this product vanish identically owing to spatial homogeneity.

Substituting these results into (A 7), the terms of leading order in $\Delta t$ give

$$\chi = 2D_{\mathrm{T}}/L^2, \tag{A 9}$$

which is analogous to (A 6) because $\nabla\Theta = 1/L$ for the configuration analysed here. The model thus obeys the key relationship that determines the overall mixing rate in terms of large-scale quantities. This is an essential property of any model intended to compute mixing properties of flow configurations specified in terms of large-scale characteristics.

Finally, some relationships involving the scalar power spectrum $E(k)$ are derived. The derivations follow Hinze (1975), with notation that encompasses both the usual three-dimensional analysis and the present one-dimensional formulation. In $d$-dimensional vector notation, a spectrum function $\tilde{S}(\boldsymbol{k})$ is defined as

$$\tilde{S}(\boldsymbol{k}) = \frac{1}{(2\pi)^d}\int S(\boldsymbol{r})\,\mathrm{e}^{-\mathrm{i}\boldsymbol{k}\cdot\boldsymbol{r}}\,\mathrm{d}\boldsymbol{r}, \tag{A 10}$$

where $S(\boldsymbol{r}) = \langle c'(\boldsymbol{x})\,c'(\boldsymbol{x}+\boldsymbol{r})\rangle$. (The reader is cautioned that slightly different definitions are adopted by some authors.) Isotropy implies that $S(\boldsymbol{r}) = S(r)$ and that the spectrum depends only on wavenumber magnitude $k$. Integrals of the spectrum over $\mathrm{d}\boldsymbol{k}$ are considered. Isotropy implies $\int\mathrm{d}\boldsymbol{k} = 4\pi\int_0^\infty k^2\,\mathrm{d}k$ for $d = 3$, and $\int\mathrm{d}\boldsymbol{k} = \int_{-\infty}^{\infty}\mathrm{d}k = 2\int_0^\infty\mathrm{d}k$ for $d = 1$. The 'three-dimensional power spectrum' $\hat{E}(k)$ is defined as $\hat{E}(k) = 4\pi k^2\tilde{S}_3(k)$, which subsumes the factor arising from the Jacobian of the transformation $\mathrm{d}\boldsymbol{k}\to\mathrm{d}k$. (The subscript indicates that the spectrum function corresponds to a three-dimensional isotropic field.) The model analogue $E(k)$ is taken to be $E(k) = 2\tilde{S}_1(k)$, which subsumes the one-dimensional Jacobian factor. (The subscript indicates that the spectrum function corresponds to a one-dimensional isotropic field in this instance.) It is important to note that this is different from the usual 'one-dimensional power spectrum', which is defined as the power spectrum obtained by applying a one-dimensional Fourier transform to the three-dimensional covariance function $S_3(\boldsymbol{r}) = S_3(r)$, and which can be expressed in terms of $\hat{E}(k)$ by means of an integral transform.

Noting that $\langle c'^2\rangle = S(0)$, integration of (A 10) over $\mathrm{d}\boldsymbol{k}$ gives $\langle c'^2\rangle = \int_0^\infty\hat{E}(k)\,\mathrm{d}k$ for $d = 3$ and the formally equivalent expression $\langle c'^2\rangle = \int_0^\infty E(k)\,\mathrm{d}k$ for $d = 1$. Noting also that $\langle c'\nabla^2 c'\rangle = \nabla^2 S(r)|_{r=0}$, the mean scalar dissipation rate $\chi \equiv 2D_{\mathrm{M}}\langle(\nabla c')^2\rangle$ can be expressed as $-2D_{\mathrm{M}}\nabla^2 S(r)|_{r=0}$ based on the relation $\langle c'(t)\,\nabla^2 c'\rangle = -\langle(\nabla c')^2\rangle$ noted earlier. Taking the inverse Fourier transform of (A 10), $\hat{\chi}$ is evaluated by applying the radial component $r^{-2}(\partial/\partial r)\,r^2(\partial/\partial r)$ of $\nabla^2$ to $S(r) = \int_0^\infty(\sin kr/kr)\,\hat{E}(k)\,\mathrm{d}k$, giving $\int_0^\infty k^2\hat{E}(k)\,\mathrm{d}k = \hat{\chi}/(2D_{\mathrm{M}})$. The one-dimensional analogue of this procedure gives the formally equivalent result

$$\int_0^\infty k^2 E(k)\,\mathrm{d}k = \chi/(2D_{\mathrm{M}}). \tag{A 11}$$

These formal equivalences involving integrals of the spectrum over $\mathrm{d}k$ and over $k^2\,\mathrm{d}k$ are the basis of the assertion in §2 that power spectra of the simulated concentration field are directly analogous to measured three-dimensional power spectra.

Equation (A 11) provides a rationale for the model analogue of Batchelor scaling, specified by (9). Substitution of (9) and the definitions of $T_\mathrm{K}$, $K_\mathrm{B}$, $L_\mathrm{B}$ and $Sc_\mathrm{S}$ into (A 11) gives

$$\int_0^\infty K_\mathrm{B}^2 E_\mathrm{B}(K_\mathrm{B})\,\mathrm{d}K_\mathrm{B} = \tfrac{1}{2}, \tag{A 12}$$

the same result that is obtained for the physical quantity $\int_0^\infty k_\mathrm{B}^2 \hat{E}_\mathrm{B}(k_\mathrm{B})\,\mathrm{d}k_\mathrm{B}$ based on the usual Batchelor scaling (Gibson 1968*b*). A value other than $\frac{1}{2}$ could have been obtained in (A 12) by choosing a coefficient other than unity in the definition of $T_\mathrm{K}$. For example, the definition $T_\mathrm{K} = L_\mathrm{K}^2/\nu$ gives $T_\mathrm{K} = [Pr_\mathrm{T}^{-1} Re/Re_\mathrm{S}]\, Re_\mathrm{S}^{\frac{1}{2}} L^2/D_\mathrm{T}$ based on foregoing definitions, where the coefficient in square brackets has an estimated value of $[(0.8)(2.5)]^{-1} = 0.50$. Were this definition adopted, the integral in (A 12) would equal unity instead of $\frac{1}{2}$, so all curves in figures 4 and 6 (including three-dimensional as well as one-dimensional results) would be shifted upward by a factor of 2.0.

## REFERENCES


Andrews, L. C., Phillips, R. L., Shivamoggi, B. K., Beck, J. K. & Joshi, M. L. 1989 A statistical theory for the distribution of energy dissipation in intermittent turbulence. *Phys. Fluids* A **1**, 999–1006.

Andrews, L. C. & Shivamoggi, B. K. 1990 The gamma distribution as a model for temperature dissipation in intermittent turbulence. *Phys. Fluids* A **2**, 105–110.

Antonia, R. A., Hopfinger, E. J., Gagne, Y. & Anselmet, F. 1984 Temperature structure functions in turbulent shear flows. *Phys. Rev.* A **30**, 2704–2707.

Antonia, R. A. & Sreenivasan, K. R. 1977 Log-normality of temperature dissipation in a turbulent boundary layer. *Phys. Fluids* **20**, 1800–1804.

Ashurst, W. T., Kerstein, A. R., Kerr, R. M. & Gibson, C. H. 1987 Alignment of vorticity and scalar gradient with strain rate in simulated Navier–Stokes turbulence. *Phys. Fluids* **30**, 2343–2353.

Baldyga, J. & Bourne, J. R. 1984*a* A fluid-mechanical approach to turbulent mixing and chemical reaction. Part I. Inadequacies of available methods. *Chem. Engng Commun.* **28**, 231–241.

Baldyga, J. & Bourne, J. R. 1984*b* A fluid-mechanical approach to turbulent mixing and chemical reaction. Part II. Micromixing in the light of turbulence theory. *Chem. Engng Commun.* **28**, 243–258.

Baldyga, J. & Bourne, J. R. 1984*c* A fluid-mechanical approach to turbulent mixing and chemical reaction. Part III. Computational and experimental results for the new micromixing model. *Chem. Engng Commun.* **28**, 259–281.

Batchelor, G. K. 1952 The effect of homogeneous turbulence on material lines and surfaces. *Proc. R. Soc. Lond.* **213**, 349–366.

Batchelor, G. K. 1959 Small-scale variation of convected quantities like temperature in turbulent fluid. Part 1. General discussion and the case of small conductivity. *J. Fluid Mech.* **5**, 113–133.

Batchelor, G. K., Howells, I. D. & Townsend, A. A. 1959 Small-scale variation of convected quantities like temperature in turbulent fluid. Part 2. The case of large conductivity. *J. Fluid Mech.* **5**, 134–139.

Broadwell, J. E. & Breidenthal, R. E. 1982 A simple model of mixing and chemical reaction in a turbulent shear layer. *J. Fluid Mech.* **125**, 397–410.

Broadwell, J. E. & Mungal, M. G. 1988 Molecular mixing and chemical reactions in turbulent shear layers. *22nd Symp. (Intl.) on Combustion*, pp. 579–587. The Combustion Institute.

CHAMPAGNE, F. H., FRIEHE, C. A., LARUE, J. C. & WYNGAARD, J. C. 1977 Flux measurements, flux estimation techniques, and fine-scale turbulence measurements in the unstable surface layer over land. *J. Atmos. Sci.* **34**, 515–530.

CLAY, J. P. 1973 Turbulent mixing of temperature in water, air and mercury. PhD thesis, University of California at San Diego.

CURL, R. L. 1963 Dispersed phase mixing: I. Theory and effects in simple reactors. *AIChE J.* **9**, 175–181.

DIMOTAKIS, P. E. 1989*a* Turbulent free shear layer mixing and combustion. *Proc. Ninth ISABE (Athens)*, pp. 58–79.

DIMOTAKIS, P. E. 1989*b* Turbulent shear layer mixing with fast chemical reactions. *Turbulent Reactive Flows* (ed. R. Borghi & S. N. B. Murthy). Lecture Notes in Engineering, vol. 40, pp. 417–489. Springer.

DIMOTAKIS, P. E., BROADWELL, J. E. & ZUKOSKI, E. E. 1990 Combustion in turbulent jets and buoyant flames. *Gas Res. Inst. Rep.* GRI 90/0154.

DOWLING, D. R. 1991 The estimated scalar dissipation rate in gas-phase turbulent jets. *Phys. Fluids* A, (in press).

DURBIN, P. A. 1980 A stochastic model of two-particle dispersion and concentration fluctuations in homogeneous turbulence. *J. Fluid Mech.* **100**, 279–302.

ESWARAN, V. & POPE, S. B. 1988 Direct numerical simulation of the turbulent mixing of a passive scalar. *Phys. Fluids* **31**, 506–520.

FULACHIER, L. & DUMAS, R. 1976 Spectral analogy between temperature and velocity fluctuations in a turbulent boundary layer. *J. Fluid Mech.* **77**, 257–277.

FRISCH, U., SULEM, P.-L. & NELKIN, M. 1978 A simple dynamical model of intermittent fully developed turbulence. *J. Fluid Mech.* **87**, 719–736.

GARRETT, C. 1983 On the initial streakiness of dispersing tracer in two- and three-dimensional turbulence. *Dyn. Atmos. Oceans* **7**, 265–277.

GIBSON, C. H. 1968*a* Fine structure of scalar fields mixed by turbulence. I. Zero-gradient points and minimal gradient surfaces. *Phys. Fluids* **11**, 2305–2315.

GIBSON, C. H. 1968*b* Fine structure of scalar fields mixed by turbulence. II. Spectral theory. *Phys. Fluids* **11**, 2316–2327.

GIBSON, C. H., ASHURST, W. T. & KERSTEIN, A. R. 1988 Mixing of strongly diffusive passive scalars like temperature by turbulence. *J. Fluid Mech.* **194**, 261–293.

GRANT, H. L., HUGHES, B. A., VOGEL, W. M. & MOILLIET, A. 1968 The spectrum of temperature fluctuations in turbulent flow. *J. Fluid Mech.* **34**, 423–442.

GURVICH, A. S. & YAGLOM, A. M. 1967 Breakdown of eddies and probability distributions for small-scale turbulence. *Phys. Fluids Suppl.* (*Proc. Kyoto Sympos. on Boundary Layers and Turbulence*), **10**, S59–S65.

HILL, R. J. 1978 Models of the scalar spectrum for turbulent advection. *J. Fluid Mech.* **88**, 541–562.

HINZE, J. O. 1975 *Turbulence*, 2nd edn. McGraw-Hill.

KERR, R. M. 1990 Velocity, scalar and transfer spectra in numerical turbulence. *J. Fluid Mech.* **211**, 309–332.

KERSTEIN, A. R. 1986 Computational study of propagating fronts in a lattice-gas model. *J. Stat. Phys.* **45**, 921–931.

KERSTEIN, A. R. 1988 A linear-eddy model of turbulent scalar transport and mixing. *Combust. Sci. Technol.* **60**, 391–421.

KERSTEIN, A. R. 1989 Linear-eddy modeling of turbulent transport. II: Application to shear layer mixing. *Combust. Flame* **75**, 397–413.

KERSTEIN, A. R. 1990 Linear-eddy modelling of turbulent transport. Part 3. Mixing and differential molecular diffusion in round jets. *J. Fluid Mech.* **216**, 411–435.

KERSTEIN, A. R. 1991*a* Linear-eddy modeling of turbulent transport. Part 4. Structure of diffusion flames. *Combust. Sci. Technol.* (in press).

KERSTEIN, A. R. 1991*b* Linear-eddy modeling of turbulent transport. Part 5. Geometry of scalar interfaces. *Phys. Fluids* A **3**, 1110–1114.

KERSTEIN, A. R. 1991*c* Linear-eddy modelling of turbulent transport. Part 7. Finite-rate chemistry and multi-stream mixing. Preprint.

KRAICHNAN, R. H. 1968 Small-scale structure of a scalar field convected by turbulence. *Phys. Fluids* **11**, 945–953.

KRAICHNAN, R. H. 1990 Models of intermittency in hydrodynamic turbulence. *Phys. Rev. Lett.* **65**, 575–578.

LESIEUR, M. 1987 *Turbulence in Fluids*. Martinus Nijhoff.

LESLIE, D. C. 1973 *Developments in the Theory of Turbulence*. Oxford University Press.

MCMURTRY, P. A. & GIVI, P. 1989 Direct numerical simulations of mixing and reaction in a nonpremixed homogeneous turbulent flow. *Combust. Flame* **77**, 171–185.

MENEVEAU, C. & SREENIVASAN, K. R. 1990 Interface dimension in intermittent turbulence. *Phys. Rev.* A **41**, 2246–2248.

MILLER, P. L. & DIMOTAKIS, P. E. 1991 Stochastic geometric properties of scalar interfaces in turbulent jets. *Phys. Fluids* A **3**, 168–177.

MONIN, A. S. & YAGLOM, A. M. 1971 *Statistical Fluid Mechanics*, vol. 1. Massachusetts Institute of Technology Press.

MONIN, A. S. & YAGLOM, A. M. 1975 *Statistical Fluid Mechanics*, vol. 2. Massachusetts Institute of Technology Press.

OTT, E. & ANTONSEN, T. M. 1989 Fractal measures of passively convected vector fields and scalar gradients in chaotic fluid flows. *Phys. Rev.* A **39**, 3660–3671.

POPE, S. B. 1985 Pdf methods for turbulent reactive flows. *Prog. Energy Combust. Sci.* **11**, 119–192.

PRASAD, R. R., MENEVEAU, C. & SREENIVASAN, K. R. 1988 Multifractal nature of the dissipation field of passive scalars in fully turbulent flows. *Phys. Rev. Lett.* **61**, 74–77.

PRASAD, R. R. & SREENIVASAN, K. R. 1990 The measurement and interpretation of fractal dimensions of the scalar interface in turbulent flows. *Phys. Fluids* A **2**, 792–807.

PRATT, D. T. 1976 Mixing and chemical reaction in continuous combustion. *Prog. Energy Combust. Sci.* **1**, 73–86.

PUMIR, A., SHRAIMAN, B. I. & SIGGIA, E. D. 1991 Exponential tails and random advection. *Phys. Rev. Lett.* **66**, 2984–2987.

REIF, F. 1965 *Fundamentals of Statistical and Thermal Physics*. McGraw-Hill.

SAWFORD, B. L. & HUNT, J. C. R. 1986 Effects of turbulence structure, molecular diffusion and source size on scalar fluctuations in homogeneous turbulence. *J. Fluid Mech.* **165**, 373–400.

SHE, Z.-S. & ORSZAG, S. A. 1991 Physical model of intermittency in turbulence: Inertial-range non-Gaussian statistics. *Phys. Rev. Lett.* **66**, 1701–1704.

SHIH, T.-H., LUMLEY, J. L. & CHEN, J.-Y. 1990 Second-order modeling of a passive scalar in a turbulent shear flow. *AIAA J.* **28**, 610–617.

SREENIVASAN, K. R. & PRASAD, R. R. 1989 New results on the fractal and multifractal structure of the large Schmidt number passive scalars in fully turbulent flows. *Physica* D **38**, 322–329.

SREENIVASAN, K. R., RAMSHANKAR, R. & MENEVEAU, C. 1989 Mixing, entrainment and fractal dimensions of surfaces in turbulent flows. *Proc. R. Soc. Lond.* A **421**, 79–108.

TAYLOR, G. I. 1921 Diffusion by continuous movements. *Proc. Lond. Math. Soc.* **20**, 196–212.

TENNEKES, H. & LUMLEY, J. L. 1972 *A First Course in Turbulence*. Massachusetts Institute of Technology Press.

THOMSON, D. J. 1990 A stochastic model for the motion of particle pairs in isotropic high-Reynolds-number turbulence, and its application to the problem of concentration variance. *J. Fluid Mech.* **210**, 113–153.

VAN ATTA, C. W. 1971 Influence of fluctuations in local dissipation rates on turbulent scalar characteristics in the inertial subrange. *Phys. Fluids* **14**, 1803–1804.

WARHAFT, Z. 1984 The interference of thermal fields from line sources in grid turbulence. *J. Fluid Mech.* **144**, 363–387.

WILKS, S. S. 1962 *Mathematical Statistics*. Wiley.